

This is a non-peer-reviewed preprint submitted to EarthArXiv.

This manuscript has been submitted for publication in Journal of Geophysical Research: Solid Earth. Please note the manuscript has yet to be formally accepted for publication. Subsequent versions of this manuscript may have slightly different content. If accepted, the final version of this manuscript will be available via the 'Peer-reviewed Publication DOI' link on the right-hand side of this webpage. Please feel free to contact any of the authors; we welcome feedback.

Denoising teleseismic data for deep Earth studies using a supervised deep-learning auto-encoder: a case study of diffracted waves from ULVZs

Stuart Russell^{1,2}, Katrin Hannemann¹, Carl Martin^{3,4}, Bennet Lindhorst¹, Waleed Esmail⁵, Christine Thomas^{1,6}

¹Institut für Geophysik, Universität Münster, Correnstraße 24, 48149, Münster, Germany

²James Cook University, 1 James Cook Drive, Douglas, QLD, 4814, Australia

³Department of Geosciences, Utrecht University, 3584 CB, Netherlands

⁴Research School of Earth Sciences, The Australian National University, 142 Mills Road, Acton, ACT, 2601, Australia

⁵Institut für Kernphysik, Universität Münster, Wilhelm-Klemm-Straße 9, 48149, Münster

⁶Geological Survey of Denmark and Greenland, 1350 Copenhagen, Denmark

Key Points:

- A supervised auto-encoder effectively separates noise and signal in teleseismic traces, elucidating otherwise obscured signals.
- Models trained only on global noise and 1D synthetics perform well in a variety of applications including outside of the training paradigm.
- The denoiser can be readily incorporated in existing seismic workflows and has apparent potential in deep Earth seismic applications.

Plain language summary

Seismic waves generated by earthquakes are used to decipher the internal structure of the Earth. However, when these signals are recorded, they are often obscured or distorted by seismic noise – in the relevant frequency range, noise from the oceans is particularly pervasive. In this paper, we provide a demonstration that a deep-learning denoiser can effectively separate recorded teleseismic data into their signal and noise parts, allowing seismic phases to be more easily identified and studied. We present a computationally efficient workflow that uses synthetic seismograms combined with real seismic noise to train an algorithm, without the need for large datasets of real seismic phase observations or computationally costly simulations. Despite having never been exposed to real seismic signals, the resulting models prove effective at extracting real seismic signal and suppressing noise. We demonstrate a number of applications and provide recommendations for how to improve the performance of the model by applying a second training stage to the original model, known as transfer learning. Using the denoising workflow, we identify new short-period observations, as well as data sampling the Hawaiian ultra-low velocity zone from a new source-receiver geometry, demonstrating tangible benefits to deep Earth seismology. We hope to encourage the use of denoising in future studies, particularly for exploratory screening.

Corresponding author: Stuart Russell, stuart.russell@jcu.edu.au

Abstract

Seismic noise, particularly the microseism generated by the oceans, is a fundamental limitation on using short period (1 - 10 s) teleseismic data to study the deep Earth. Deep learning auto-encoders have proven effective at denoising seismic data in other applications. Here, we provide a demonstration of their potential for improving the quality of deep Earth seismic data, using S_{diff} post-cursors generated by ultra-low velocity zones as a case study. We present a computationally efficient and accessible workflow, utilising a supervised learning process with 1D synthetics and real, global seismic noise. This workflow does not require real teleseismic signals, which are limited in number and quality, and is computationally efficient, not requiring expensive 3D spectral-element simulations. We present a series of example applications, finding the denoiser to be effective at removing noise and extracting S_{diff} signal despite having not been trained with real teleseismic signals. Furthermore, we provide recommendations on how performance could be improved, including demonstrating transfer learning as an efficient and effective way to improve extraction of specific signals. Lastly we apply denoising to data sampling ULVZs, revealing observations of new short-period signals as well as sampling the Hawaiian ultra-low velocity zone using a novel source-receiver geometry from the East Pacific Rise to Japan. The potential impact of denoising deep Earth seismic data is apparent, and denoising can be implemented alongside traditional methods, such as stacking. We hope to encourage the use of deep learning denoising in future studies, particularly for exploratory screening.

1 Introduction

All seismic recordings contain noise. For seismic studies of the deep Earth, which typically use teleseismic arrivals from distant earthquakes to constrain the planet’s internal structure, noise originates from a variety of different processes, both natural and anthropogenic. Examples of these processes include weather events such as storms, ocean waves, vehicle traffic, infrastructure such as wind farms, the seismic instrument itself, as well as many others (e.g. Bormann & Wielandt, 2013). Noise obscures and distorts the seismic signal and is a fundamental limitation on the use of seismic data. Typically, deep Earth seismologists use spectral filtering to isolate signals in a period band where noise is minimal, but this method is not effective when both signal and noise occur in the same period band. Where several seismic stations are available in a region, array methods such as stacking can be used to suppress incoherent noise (Rost & Thomas, 2002, 2009; Schweitzer et al., 2012), usually in conjunction with spectral filtering. Other methods for suppressing noise and extracting signal exist, including ensemble empirical mode decomposition (Han & van der Baan, 2015), wavelet based methods (Gaci, 2013; Mousavi et al., 2016; Langston & Mousavi, 2019), and the use of deep-learning, but these do not currently have common usage in deep Earth seismology.

Deep-learning denoisers in particular have received significant recent attention and have been shown to be effective in a wide variety of seismic applications, outperforming alternatives (e.g. Zhu et al., 2019; Heuel & Friederich, 2022; Tibi et al., 2023). Example uses to date include denoising regional-distance seismic data (Tibi et al., 2021), ocean bottom seismometers (Lin et al., 2024), offshore distributed acoustic sensing cables (Shi et al., 2025), ambient seismic field correlation functions (Viens & Van Houtte, 2020), microseismic event detection (e.g. Othman et al., 2021; Ma et al., 2023), observing deep Earthquake rupture (Shi & Denolle, 2023), downhole microseismic monitoring (Ge et al., 2024), seismic exploration (J. Li et al., 2023), nuclear monitoring (Steinberg et al., 2024), removal of anthropogenic noise (Heuel & Friederich, 2022; Yang et al., 2022), and for Martian seismology (Dahmen et al., 2022, 2024). Unsupervised deep-learning denoisers have been applied to improve receiver functions (Dalai et al., 2022; Feng et al., 2024), and recently to weak PcP signals (Oboué et al., 2026), but otherwise the use of deep-learning denoisers in deep Earth seismic studies is thus far limited, despite their potential to be highly impactful. In this study, we assess the potential of a supervised time-frequency domain denoising auto-encoder for denoising teleseismic data, using Ultra-low Velocity Zones (ULVZs) as a case study.

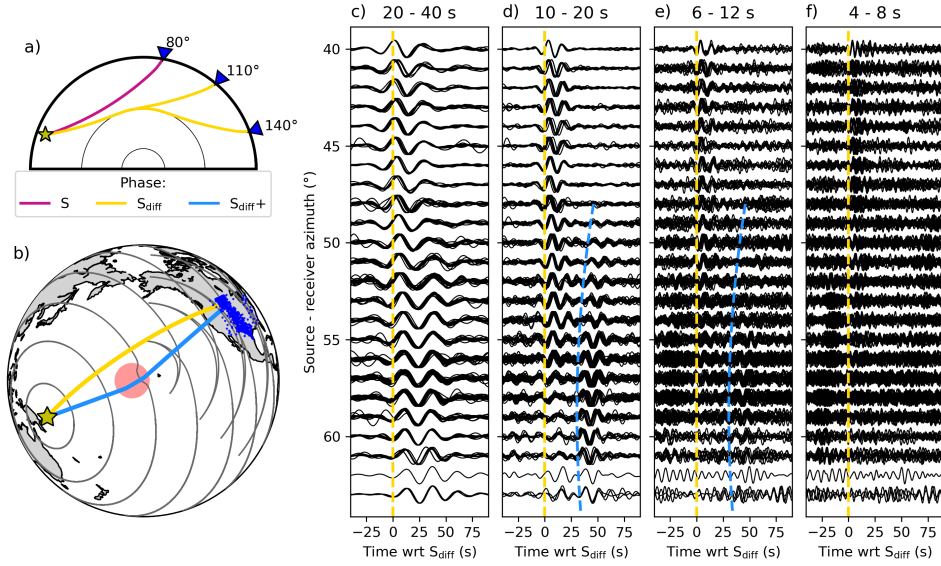


Figure 1. An introduction to S_{diff} and $S_{\text{diff}+}$. a) Example ray paths of S and S_{diff} in a cross-section of the Earth. b) Example ray paths and wavefronts of S_{diff} and $S_{\text{diff}+}$ in plan view for an earthquake in Papua New Guinea to stations the US, with the location of the Hawaiian ULVZ marked (Cottaar & Romanowicz, 2012). Wavefronts, curved by the ULVZ, are marked in grey. c) - f) Example waveforms for the source-receiver geometry shown in b) of Event 20100320. The same data are filtered in four different octave-width filter-bands as indicated. Arrival times of S_{diff} and $S_{\text{diff}+}$ are marked where visible. All traces are individually normalised and displayed rounded to the nearest degree of azimuth.

83 The core-mantle boundary (CMB) separates the solid silicate mantle from the liquid iron-alloy
84 core at a depth of approximately 2890 km within the Earth (Oldham, 1906; Dziewonski & Anderson,
85 1981). The region approximately 200 - 300 km thick above the CMB is the lower thermal boundary
86 layer of the convecting mantle and hosts significant seismic heterogeneity, of which ULVZs are the most
87 extreme features. ULVZs are highly anomalous structures of severely reduced S-velocities – reported
88 to be up to 50% slower than the background mantle – that sit atop the CMB (for overviews see e.g.
89 Yu & Garnero, 2018; McNamara, 2019; Jackson & Thomas, 2021). They are typically only tens of kilo-
90 metres thick but can be hundreds to thousands of kilometres in diameter (Cottaar & Romanowicz,
91 2012; Thorne et al., 2013; Yuan & Romanowicz, 2017; Cottaar et al., 2022). The formation mecha-
92 nisms, composition, physical state and internal structure of ULVZs are all poorly understood; as is
93 their relationship to other observed structures in the mantle, as well as to the dynamics of both the
94 core and mantle. The key to better understanding ULVZs and their place in the Earth system is by
95 better resolving their distribution, morphology and relationship to other structures.

96 One way to study ULVZs is with S_{diff} post-cursors. S_{diff} is a shear wave that diffracts along the
97 CMB (Figure 1a). The vertically polarised S_V energy attenuates rapidly, while the horizontally po-
98 larised S_H is readily observed on the transverse (T) components of seismograms from approximately
99 100° to 130° epicentral distance. When S_{diff} encounters a ULVZ, the wave is lensed by the velocity con-
100 trast (Figure 1b), leading to a secondary arrival of energy. This secondary arrival is clear when S_{diff}
101 arrivals are viewed as a function of source-to-receiver azimuth (Figure 1c-f), and is known as an S_{diff}
102 post-cursor or $S_{\text{diff}+}$ (Cottaar & Romanowicz, 2012; Martin et al., 2023a).

103 Here, we consider some challenges faced by seismologists analysing S_{diff} and $S_{\text{diff}+}$ and highlight
104 opportunities for inclusion of the DAE within existing workflows to potentially address these challenges.
105 A major challenge is that the screening of record sections for $S_{\text{diff}+}$ remains a laborious process, typ-
106 ically involving expert examination of record sections (e.g. Martin et al., 2023a; Atkins et al., 2026),
107 in which the visibility of $S_{\text{diff}+}$ depends on processing steps and signals can easily be overlooked – de-
108 noising provides a complementary perspective on this data. Beyond the screening stage, the behaviour
109 of $S_{\text{diff}+}$ is frequency dependent. Observations of signals at shorter period can reveal the internal struc-
110 ture of ULVZs (e.g. Z. Li et al., 2022) and also facilitate the discovery of new ones (e.g. Martin et al.,
111 2024), but observations at periods < 10 s are challenging due to the high noise level (e.g. Figure 1).
112 The dominant noise in this period range is the microseism, which is mid- to short-period noise gen-
113 erated by the coupling of the solid Earth with the oscillating oceans (e.g. Longuet-Higgins, 1950; Dar-
114 byshire, 1950; Iyer, 1958; Friedrich et al., 1998). There is also a coverage challenge as there are fewer
115 and more widely spaced seismometers deployed in the southern hemisphere. There is an over-reliance
116 on stations in North America and Europe in particular, leading to over-sampling of certain regions
117 of Earth’s interior. Denoising can allow the use of lower quality data in regions with characteristically
118 higher noise levels, such as ocean bottoms, ocean islands, or polar regions. In this way, it may be pos-
119 sible to sample more of the CMB in the search for ULVZs.

120 In this study, we use a deep-learning denoising auto-encoder (DAE) to denoise S_{diff} and $S_{\text{diff}+}$
121 waveforms that sample several different known ULVZs. We present a computationally efficient and
122 accessible training workflow that uses Instaseis synthetics and real, global noise – thus not requiring
123 computationally expensive 3D waveform simulations or data sets of real seismic phases. By using dif-
124 ferent variations of this training data, we attempt to ascertain the conditions in which the denoiser
125 works well and how performance can be improved. We demonstrate the efficacy of denoising by ap-
126 plying to S_{diff} data, revealing observations of short-period signals from various ULVZs, and identify-
127 ing data sampling the Hawaiian ULVZ using a novel source-receiver geometry. Finally, we discuss pos-
128 sible applications, and outline some recommendations for usage based on our experiences. We hope
129 to encourage wider use of denoising in deep Earth seismology, particularly for screening, and, while
130 this study uses S_{diff} and ULVZs as a case study, we envision denoising proving useful across a wide
131 range of other deep Earth seismic applications.

2 Methods

2.1 Representation of signals

Our denoiser is based on the DAE model of Zhu et al. (2019), as implemented by Heuel & Friederich (2022) for removing noise generated by windfarms. Auto-encoders are a class of deep learning algorithms that aim to learn a sparse or latent representation of an input to extract specific features. The DAE comprises of two connected parts: the encoder compresses an input image through several convolutional layers into a latent space, while the decoder expands this latent representation back to its original dimensions through the same number of deconvolutional layers. This two-stage process allows the extraction of key features from the input image, and the accurate reconstruction of these key features in the output image. In the case of the DAE, the input is a time-frequency representation of a seismic trace and the aim is separate this into two independent parts: the signal and the noise.

In body wave studies of the deep Earth, teleseismic data are visualised foremost in the time domain, and a seismic trace, $y(t)$, can be viewed as the superposition of seismic signal time series, $s(t)$, containing the signal of interest, and a seismic noise time series, $n(t)$, that contains any number of other seismic oscillations that are not of interest,

$$y(t) = s(t) + n(t). \quad (1)$$

The terms signal and noise are relative and will vary between different seismologists, studies and applications. A seismic trace can be transformed into the time-frequency domain by application of some time-frequency transform, TFFT,

$$X(t, f) = \text{TFFT}\{x(t)\}, \quad (2)$$

where x and X represent any seismic trace and the time-frequency representation of that trace. In the time-frequency domain the summation of signal and noise is equivalent to the time domain

$$Y(t, f) = S(t, f) + N(t, f). \quad (3)$$

The objective of the DAE is to decompose the input signal, Y , into approximations of S and N , denoted as \hat{S} and \hat{N} , respectively. \hat{S} is calculated from Y by

$$\hat{S}(t, f) = \hat{M}_S(t, f) Y(t, f), \quad (4)$$

and \hat{N} in the same fashion

$$\hat{N}(t, f) = \hat{M}_N(t, f) Y(t, f), \quad (5)$$

where \hat{M}_S and \hat{M}_N are estimations of two mask functions, M_S and M_N , defined as

$$M_S(t, f) = \frac{1}{1 + \frac{|N(t, f)|}{|S(t, f)|}} \quad (6)$$

and

$$M_N(t, f) = \frac{\frac{|N(t, f)|}{|S(t, f)|}}{1 + \frac{|N(t, f)|}{|S(t, f)|}} = 1 - M_S(t, f). \quad (7)$$

157 These mask functions have values between 0 and 1, and map each part of the time-frequency repre-
 158 sentation Y to the signal or noise. It is these mask functions that the algorithm seeks to learn. The
 159 training process is a supervised one where known signal and noise time series are summed, the time-
 160 frequency transforms calculated, and the algorithm optimises the process of separating these into the
 161 original parts.

162 It is worth noting two important implications of using mask functions rather than attempting
 163 to directly learn signal and noise. The first is that as the mask functions have a maximum value of
 164 1 and are multiplied by Y , the outputs \hat{S} and \hat{N} cannot have amplitudes larger Y . This means that
 165 DAE cannot erroneously produce large amplitude signals where they are not already present. The sec-
 166 ond is that as the mask functions are applied equally to the real and imaginary parts of Y , the phase
 167 of Y is preserved in \hat{S} and \hat{N} . This limits any time shifts or waveform distortion that can result from
 168 the application of the DAE.

169 The choice of time-frequency transform to use, as well as the length and sampling rate of the
 170 time series, are important parameters for the implementation of the DAE as they influence the size
 171 and resolution of the images used for learning. In this paper, the input time series all have a length
 172 of 600 s sampled at 5 Hz, therefore with a length of 3001 samples, which is appropriate for teleseis-
 173 mic data. For the time-frequency transform we follow Zhu et al. (2019) and Tibi et al. (2021) and use
 174 the short-time Fourier transform (STFT); this is as effective as and more efficient than the contin-
 175 uous wavelet transform (Heuel & Friederich, 2022). The STFT images used, and thus also the size
 176 of the mask functions, is 199×61 , with 199 frequency points spanning 0 - 2.5 Hz with an interval of
 177 0.013 Hz, and 61 time points spanning 0 - 600 s with an interval of 10 s.

178 2.2 Generation of training data

179 For the supervised training process we require high-quality examples of both signal and noise.
 180 For seismic noise there is no shortage of training data as most recorded seismograms are composed
 181 predominantly of noise. For teleseismic signal, however, there is a shortage of high-quality recordings.
 182 This is especially true when considering the often small (10^2 - 10^5 waveforms) datasets of specific deep
 183 Earth phases. Even where datasets are available, they are contaminated with noise, which will im-
 184 pede the learning process. In this paper we will circumvent this issue by using only synthetic signals
 185 to train the DAE (Mousavi & Beroza, 2022), an approach that has been successfully employed for other
 186 recent deep Earth machine learning applications (e.g. Zhou et al., 2024).

187 2.2.1 Noise datasets

188 We first construct a worldwide noise dataset using stations from the Global Seismographic Net-
 189 work (GSN; Romanowicz & Dziewonski, 1987; Ringler et al., 2020, 2022; Wilson et al., 2024). The
 190 GSN is a globally distributed seismic network currently comprising ~ 140 stations, many of which have
 191 over 30 years near-continuous recording (see Supplementary Section S2 for more details). Using the
 192 ObsPy FDSN web-service (Beyreuther et al., 2010) we download seismic data for network codes CU,
 193 IC, II, and IU, selecting random 600 s second long time windows, starting from the deployment date
 194 of each station to the decommissioning date, or to September 2025 if the station is still active. As we
 195 are primarily interested in S_{diff} , we download only the horizontal components (north and east); across
 196 these two components, not accounting for outages, there would be > 8000 years of possible seismic data.

197 While these seismograms are expected to be predominantly noise, some of the randomly selected
 198 time windows will contain seismic signal, which will contaminate the noise dataset. To minimise this
 199 contamination we use an STA/LTA discrimination process with an STA length of 100 samples, an LTA
 200 length of 1000 samples, and reject traces that have any STA/LTA values exceeding 5. Our final dataset

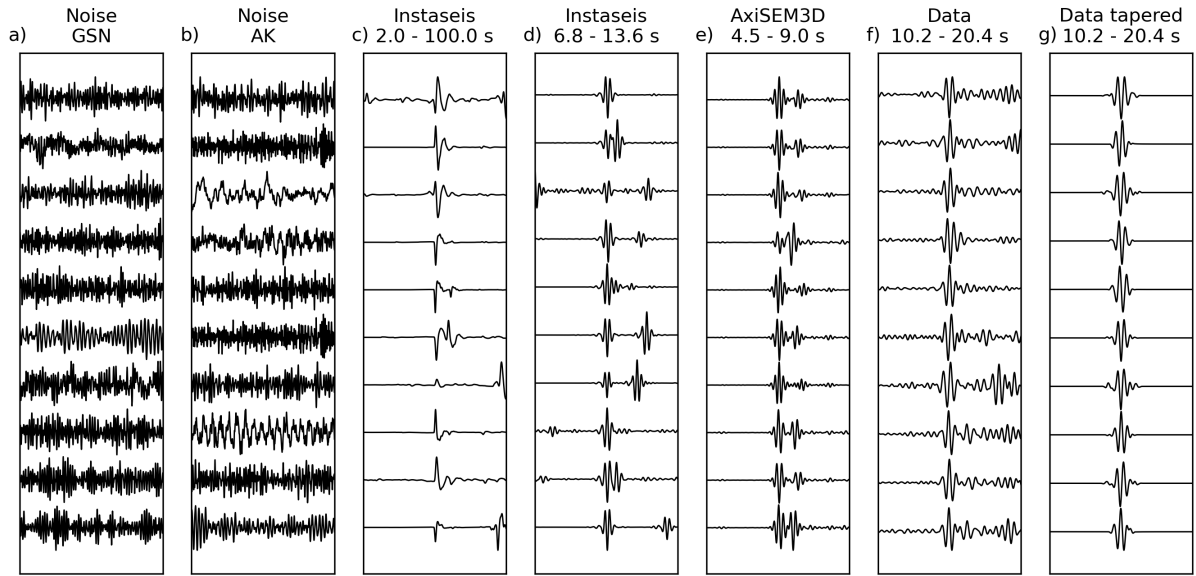


Figure 2. Example traces from various training datasets. a) Noise from the GSN; b) noise from the AK array in Alaska; c) Instaseis synthetics filtered 2 - 100 s; d) Instaseis synthetics filtered 6.8 - 13.6 s; e) AxiSEM3D synthetics with a ULVZ filtered 4.5 - 9.0 s; f) real data filtered 10.2 - 20.4 s; g) real data filtered 10.2 - 20.4 s with a taper applied around the S_{diff} signal. All traces are individually normalised. Only the central 300 s of each trace is shown.

201 comprises 512,000 individual traces, which is $\sim 0.12\%$ of the possible available traces, assuming no over-
 202 laps or outages, for the GSN. Using this workflow we can also construct region- or network-specific
 203 noise datasets. Example noise traces are shown in Figure 2a and 2b.

204 2.2.2 Synthetics - Instaseis

205 Synthetic seismograms for a particular model of the Earth can be calculated using spectral-element
 206 simulations of seismic wave propagation (e.g. Komatitsch & Tromp, 1999; Chaljub et al., 2007). How-
 207 ever, these are computationally extremely costly and computation time scales with frequency to the
 208 power of 3 - 4, depending on the parameterisation used (Leng et al., 2019). For global simulations at
 209 relevant periods, these simulations can take thousands or even millions of CPU hours per hour of seis-
 210 mogram (e.g. Komatitsch, 2011; Nissen-Meyer et al., 2014; Leng et al., 2019). Generating synthetic
 211 training data can therefore be very costly if done from scratch.

212 A large part of this computational cost can be avoided by using Instaseis (van Driel et al., 2015),
 213 a Python package that accesses pre-computed Green's function databases, calculated using AxiSEM
 214 (Nissen-Meyer et al., 2014), and generates synthetic seismograms for 1D Earth models near instan-
 215 taneously by utilising the reciprocity of the Green's functions. We use the anisotropic version of the
 216 Preliminary Reference Earth Model (PREM; Dziewonski & Anderson, 1981), PREM_a_2s, hosted by
 217 Syngine (Hutko et al., 2017; Krischer et al., 2017). This database has a minimum valid period of 2 s,
 218 controlled by the mesh spacing during computation, and a maximum valid period of 100 s, due to the
 219 neglect of full-gravity by application of the Cowling approximation (Komatitsch & Tromp, 2002; van
 220 Driel et al., 2021); the synthetics must therefore be filtered from 2 - 100 s as a minimum requirement,
 221 but can be filtered to more specific period bands within these limits to encourage the extraction of
 222 signal of a specific frequency. We create datasets for six overlapping octave-width filter-bands, every
 223 half octave from 2 s. This covers the range of previous ULVZ observations with S_{diff} .

224 We generate traces such that each 600 s long trace has a synthetic T-component seismic arrival
 225 at the centre. To increase the diversity of the training data we do not limit ourselves to S_{diff} , but also
 226 include S and SS arrivals with an epicentral distance between 50° and 130° , source depths down to
 227 600 km, and randomly generated but realistic moment tensors. Example Instaseis traces are shown
 228 in Figure 2c and 2d.

229 **2.2.3 Synthetics - AxiSEM3D**

230 By using Instaseis we save a significant computational cost, but are limited to 1D Earth mod-
 231 els that do not contain any 3D structure, including ULVZs. The Instaseis synthetics thus only con-
 232 tain S_{diff} and not $S_{\text{diff}+}$, and are unlike real seismic data that have interacted with a highly hetero-
 233 geneous mantle. We therefore also calculate 3D synthetics using AxiSEM3D (Leng et al., 2016, 2019),
 234 which has been used extensively to model $S_{\text{diff}+}$ and other ULVZ-associated seismic signals (e.g. Z. Li
 235 et al., 2022; Wolf & Long, 2023; Martin et al., 2024; Jagt et al., 2024; Wolf et al., 2024).

236 Due to the high computational cost, even with optimised inputs (following Russell et al., 2025),
 237 we only run a single AxiSEM3D simulation with a minimum period of 4 s. Our AxiSEM3D training
 238 dataset therefore only has a single source depth and a single set of ULVZ parameters, and does not
 239 contain 3D structure except for the ULVZ. We use a source depth of 500 km for a 3D model contain-
 240 ing a cylindrical ULVZ (radius: 400 km; height: 20 km; S-velocity reduction: 20%) embedded on top
 241 of the core-mantle boundary within PREM. See Supplementary Section S3 for further details on the
 242 AxiSEM3D simulation. Example AxiSEM3D traces are shown in Figure 2e.

243 **2.2.4 Real S_{diff} data**

244 Our final training dataset utilises real S_{diff} traces recorded in the contiguous USA. From the Mar-
 245 tin et al. (2023a) dataset of S_{diff} record sections that sample of Hawaiian ULVZ, we screen the data
 246 by eye and manually select traces that have high SNR S_{diff} arrivals in the 10 - 20 s period-band, giv-
 247 ing 724 traces from 30 different earthquakes recorded in the contiguous US. Only the quality of S_{diff} ,
 248 not $S_{\text{diff}+}$, is considered when selecting traces. We allow traces to be repeated and augment each trace
 249 in the frequency domain by implementing a random phase shift. We generate an augmented train-
 250 ing dataset of 51,200 traces. These traces contain contaminating noise, and to assess the effect of this
 251 we create a further training dataset. For this dataset, a taper of variable length is applied centred on
 252 the S_{diff} peak which removes all noise along with any subsequent $S_{\text{diff}+}$ arrivals. Example traces from
 253 both of these datasets are shown in Figure 2f and 2g.

254 **2.3 Model setup**

255 The DAE is built in Python using the TensorFlow software library and our model setup follows
 256 that used by Heuel & Friederich (2022). The two input layers are the normalised real and imaginary
 257 parts of the STFT of a seismic trace. The two output layers are the estimates of the two mask func-
 258 tions, \hat{M}_S and \hat{M}_N . The targets, M_S and M_N , are calculated directly from the training data using
 259 Equations (6) and (7), and the model is optimised by minimising a loss function, ℓ ,

$$\ell = \frac{\ell_S + \ell_N}{2}, \quad (8)$$

260 where ℓ_S and ℓ_N are the mean binary cross-entropy loss for the signal and noise masks, respectively,
 261 and

$$\ell_X = \frac{1}{2N_0N_1} \sum_{i=0}^{N_0} \sum_{j=0}^{N_1} M_{X_{ij}} \log \hat{M}_{X_{ij}} + (1 - M_{X_{ij}}) \log (1 - \hat{M}_{X_{ij}}), \quad (9)$$

262 where X denotes whether the masks are for signal or noise, and the mask function images (and the
263 input STFT images) have size $N_0 \times N_1$, where N_0 is the number of samples along the frequency axis,
264 and N_1 is the number of samples along the time axis – in this application 199×61 .

265 The encoder reduces the dimensions of the input layers and consists of six 2D convolutional lay-
266 ers with kernel size of 3×3 and stride length of 2×2 , each followed by a leaky rectified linear unit
267 (ReLU) activation function, batch normalisation (BN) (Ioffe & Szegedy, 2015), and a dropout layer
268 (Srivastava et al., 2014) with a drop rate of 0.1. The setup of the decoder is the inverse of the encoder
269 and increases the dimensions of the sparse representation to obtain the two output masks. 2D decon-
270 volutional layers are followed by cropping, leaky ReLU, BN, and dropout. The final layer undergoes
271 a further 2D convolution with a kernel size of 1×1 and a softmax activation function (Bridle, 1990)
272 to generate the mask functions. As in previous implementations of this algorithm we also use skip con-
273 nections to improve convergence (Ronneberger et al., 2015; Liu & Yang, 2018). With this configura-
274 tion, the DAE has 1,183,002 trainable parameters.

275 2.4 Training process

276 During training, the data are randomly split into 80% for training and 20% for validation. We
277 train our model on a single NVIDIA GeForce RTX 4090 GPU on the PALMA-II cluster of the Uni-
278 versity of Münster. We use a batch size of 32 traces; each batch is generated by selecting noise traces
279 and signal traces at random from the pool of traces that have not been used yet that epoch. Traces
280 are first demeaned and normalised and then random time shifts of up to ± 300 s are applied to the
281 signal traces, which are then cut and zero-padded to the original length. The traces are scaled such
282 that either signal or noise is up to 3 times larger amplitude than the other. The signal and noise are
283 then summed to make a trace of ‘noisy signal’, which is again demeaned and normalised such that the
284 absolute maximum amplitude has value 1 – this normalisation is essential for the convergence of the
285 algorithm. In order to help the model identify pure noise we also sometimes set the entire signal trace
286 amplitude to zero with an occurrence of 1%. Finally the input layers are calculated by taking the real
287 and imaginary parts of the STFT of each trace. We use an Adam optimiser with a learning rate of
288 10^{-6} . We train our model for a maximum of 200 epochs and if the loss of the validation data does not
289 improve for 10 successive epochs then training is stopped early. We have explored various hyper-parameter
290 combinations including different batch sizes, learning rates and numbers of convolutional layers, set-
291 tling on a configuration that gives stable learning curves, with sufficient validation loss in a reason-
292 able training time-frame. Training typically takes 1 - 2 days.

293 As well as simply running a single training process, by which a model is optimised from a set
294 of random initial weights, it is also possible to start from a previously trained model and update the
295 weights for a new but related task – this is known as transfer learning (e.g. Weiss et al., 2016). Trans-
296 fer learning allows computationally efficient training for tasks with relatively few training data, as the
297 majority of the learning can be done with the first training step. The second training step is also typi-
298 cally much faster, as the learning distance from the starting model to the final model is shorter. In
299 this way, a model trained on noise from the GSN could be retrained for a specific network with less
300 available data. Alternatively, a model trained with Instaseis synthetics could be retrained with a smaller
301 dataset of AxiSEM3D synthetics or even real data. During retraining we freeze the weights of the en-
302 coder, allowing only the decoder to retrain, which preserves the earlier layers typically responsible for
303 feature extraction (Iman et al., 2023). To prevent over-fitting, the transfer learning stage has the same
304 early stopping criterion as for the original training. A schematic demonstrating the two-step train-
305 ing process is shown in Figure 3.

306 2.5 Test S_{diff} data

307 Using the ObsPy FDSN web-service (Beyreuther et al., 2010) and HinetPy (Tian, 2024), we down-
308 load a number of T-component seismic record sections from 2000 to 2024 that contain clear S_{diff} ar-
309 rivals. Many of these also contain $S_{\text{diff}+}$ arrivals associated with the Hawaiian (Cottaar & Romanow-
310 icz, 2012; Z. Li et al., 2022; Martin et al., 2023a), Galápagos (Cottaar et al., 2022), Pitcairn (Z. Li

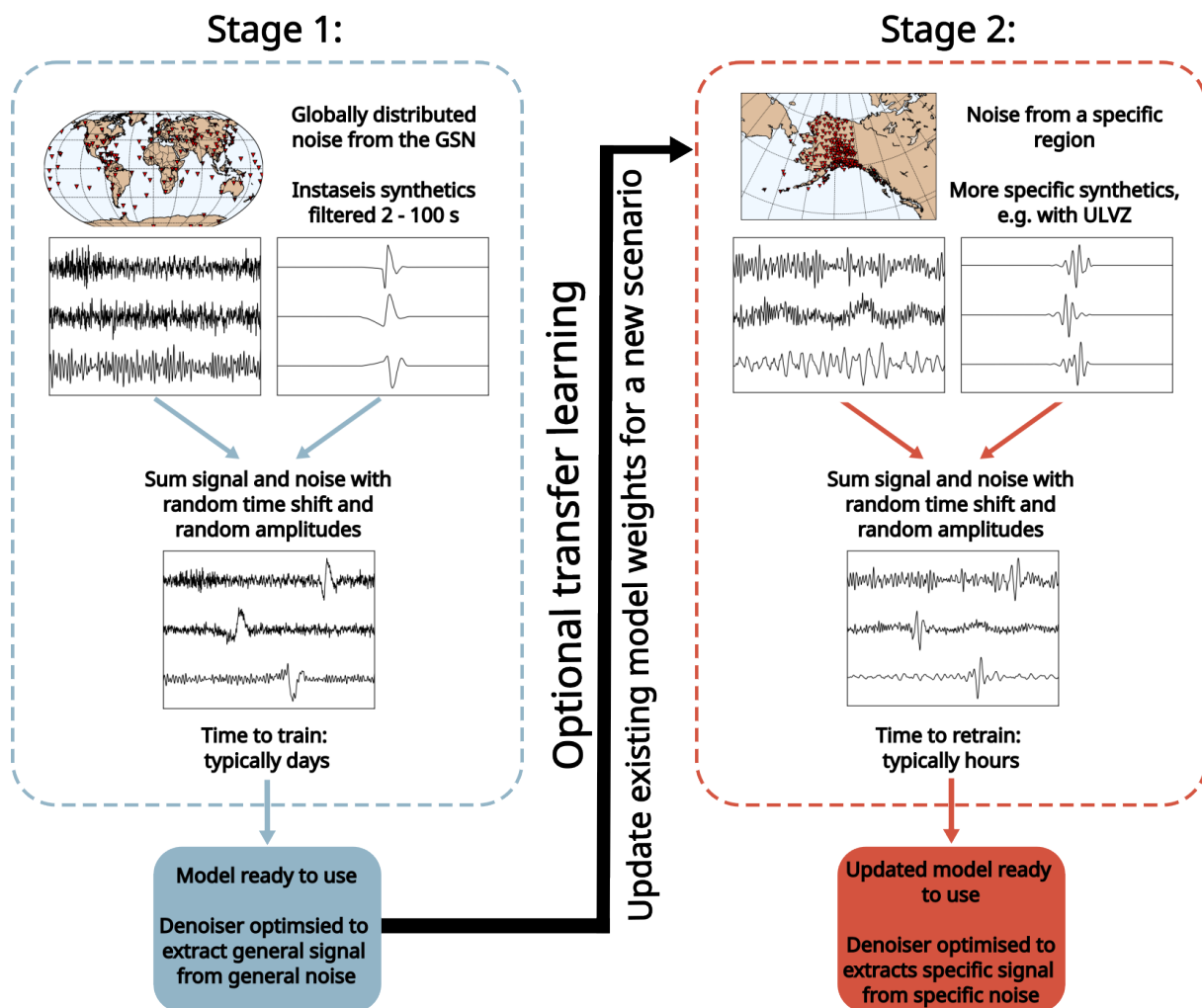


Figure 3. A flow chart demonstrating the transfer learning process. Training can be ended after either stage.

311 et al., 2024), Central Pacific (Martin et al., 2024) and Vanuatu (Martin et al., 2025) ULVZs. Station
 312 locations vary, but are mostly in the contiguous US, Alaska and Japan. As with the training data,
 313 these traces are 600 s long and sampled at 5 Hz. These record sections form the test dataset by which
 314 we will assess the performance of the trained DAE models on real data.

315 3 Verification and testing results

316 3.1 1D synthetic testing

317 Before application to real S_{diff} record sections, we first benchmark a trained DAE model against
 318 synthetic test datasets. The first tests are performed on an unseen dataset of 10,000 S_{diff} Instaseis syn-
 319 thetics and 10,000 noise traces from the US Transportable Array (FDSN network code TA), constructed
 320 in the same fashion as the original training data. The aim of these tests is to verify that the DAE has
 321 learned its task adequately, and to assess its performance over a range of noise levels. Noise level is
 322 defined by specifying a peak amplitude ratio, where during summation the signal and noise are nor-
 323 malised at a fixed ratio. An amplitude ratio of 1 is where the signal and noise have the same max-
 324 imum amplitude, an amplitude ratio of 2 is where the signal has twice the amplitude of the noise, and
 325 so on. During summation, the signal is randomly shifted to test performance regardless of the loca-
 326 tion of signal within the trace.

327 A summary of the results are shown in Figure 4, with further detailed results presented in Sup-
 328plementary Section S4. We quantify timing errors by cross-correlating the recovered and original traces,
 329 taking the maximum correlation to be the signal location, and we quantify amplitude errors by cal-
 330culating the mean-squared-error (MSE) between the input and recovered signal traces,

$$\text{MSE} = \frac{1}{n} \sum^n (s(t) - \hat{s}(t))^2, \quad (10)$$

331 where $s(t)$ is the input signal, $\hat{s}(t)$ is the recovered signal, and n is the number of test traces, in this
 332 case 10,000. The MSE is calculated for a 20 s window around the phase arrival so that amplitude dif-
 333ferences are explicitly quantified for the S_{diff} phase itself.

334 Across all three amplitude ratios shown, the signal is typically visually well-extracted. There is
 335 a visible reduction in performance at higher noise levels and there is also an associated broadening
 336 of the error distributions. The median absolute time shift is 0 or 1 samples (sampling rate is 5 Hz)
 337 for amplitude ratios down to 0.5, so where signal is half the amplitude of the noise. For smaller am-
 338 plitude ratios the median error increases rapidly as the DAE fails to extract the signal at all. For all
 339 amplitude ratios tested, the most common absolute time shift is always 0 or 1 samples, indicating that
 340 even where errors are more likely in noisier data, the most common outcome is no significant time shift.

341 These results indicate that for reasonable noise levels, signal is accurately extracted, but errors
 342 are lower where the noise level is already low. This is unsurprising as signal that is already visible is
 343 clearly going to be easier for the DAE to identify. While these results suggest that the DAE is bet-
 344 ter at ‘tidying up’ noisy data rather than uncovering signal that is totally obscured by noise, the DAE
 345 certainly demonstrates remarkable aptitude for the latter. Signal with an amplitude ratio of 0.5, as
 346 shown in Figure 4a, would likely be considered devoid of signal with traditional visual screening, and
 347 those with an amplitude ratio of 1.0 would be considered ambiguous. That the DAE can elucidate these
 348 signals, indicating where hidden signals may be present even if extraction is not point-for-point ex-
 349 act, is remarkable and suggests that the DAE has learned well within its training paradigm.

350 3.2 3D synthetic testing

351 To test generalisation beyond the training distribution, we apply the Instaseis-trained DAE to
 352 AxiSEM3D synthetics that contain S_{diff} arrivals not present in the training data. These are the same
 353 AxiSEM3D synthetics described in Section 2.2.3 and Supplementary Section S3 and these have not

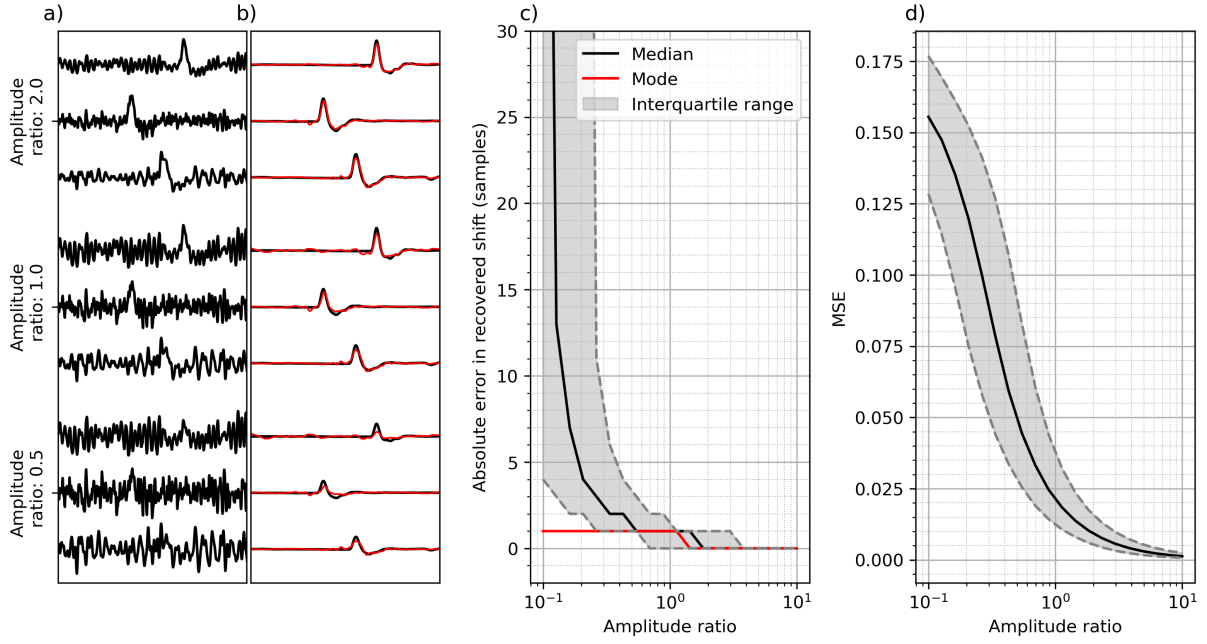


Figure 4. Synthetic testing results on unseen noise and Instaseis synthetics. a) The input signal that is the sum of an Instaseis S_{diff} arrival and noise from the US Transportable Array, for three different amplitude ratios. b) The input (black) and recovered (red) signal. c) The best-fitting shift in the recovered traces measured by cross-correlation, quantifying timing errors as a function of the imposed amplitude ratio. d) As for c), but showing the MSE between the input and recovered signal traces, quantifying amplitude errors.

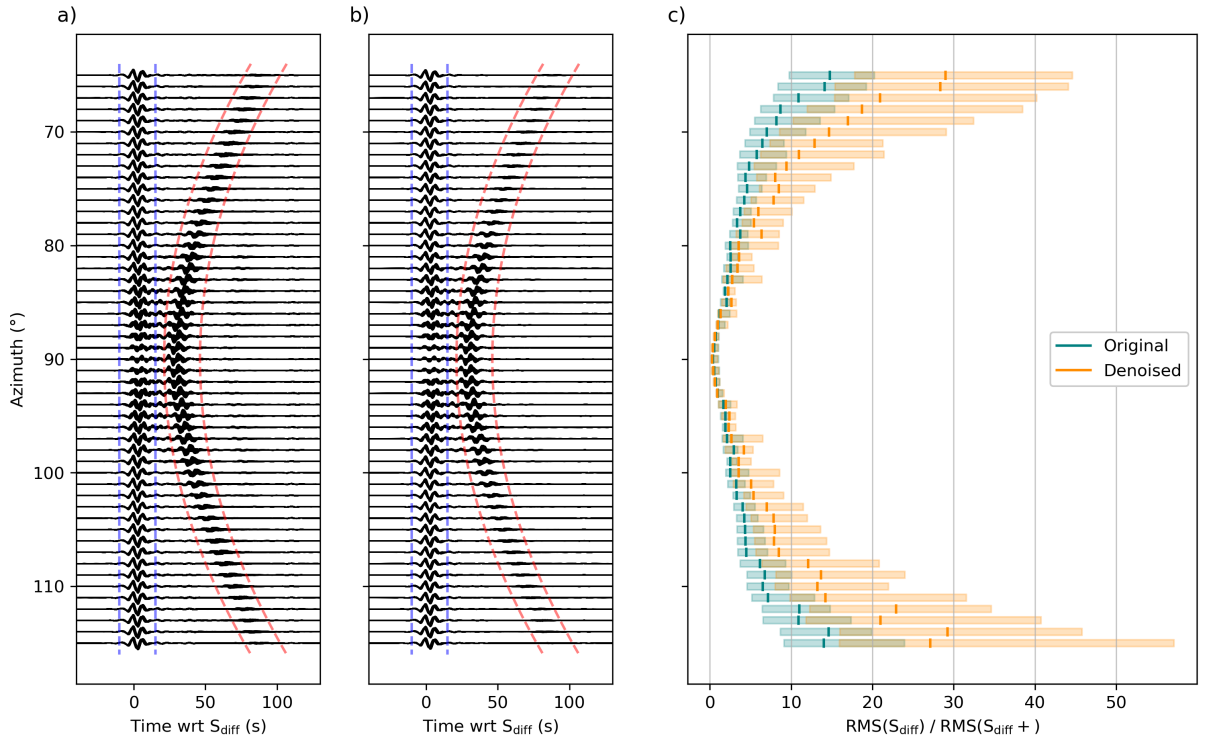


Figure 5. a) Input clean AxiSEM3D synthetics, b) the denoised synthetics. The blue and red dashed lines mark the 5 s long windows used for calculating the RMS of S_{diff} and $S_{\text{diff}+}$, respectively. c) The RMS ratio of S_{diff} to $S_{\text{diff}+}$ for the original synthetics (teal) and the denoised synthetics (orange). The lines show the median for each 1° wide azimuth bin, and the shaded boxes show the interquartile range.

354 been used to train this particular DAE. The aim of this test is to assess the performance of the DAE
 355 at extracting signals that it has not explicitly been trained to extract.

356 We use the DAE to denoise clean AxiSEM3D synthetics, so any discrepancies before and after
 357 denoising are due to the DAE itself. Results are shown in Figure 5, and further results with noise are
 358 presented in Supplementary Section S5. Qualitatively, we find that the DAE trained on Instaseis syn-
 359 thetics does satisfactorily extract the $S_{\text{diff}+}$, as shown by the likeness of the input and recovered syn-
 360 thetics shown in Figure 5a and 5b. We quantitatively assess the relative performance on S_{diff} and $S_{\text{diff}+}$
 361 by comparing the root-mean-square (RMS) amplitude of a 5 s long time window around each phase.
 362 As is expected, the off-axis $S_{\text{diff}+}$ is lower amplitude and the ratio $\text{RMS}_{S_{\text{diff}}} / \text{RMS}_{S_{\text{diff}+}}$ correspond-
 363 ingly has higher values off-axis. However, in the denoised synthetics this is even more exaggerated,
 364 indicating that off-axis $S_{\text{diff}+}$ is partially suppressed by the DAE.

365 This is unsurprising as off-axis $S_{\text{diff}+}$ is most distorted by the ULVZ and is farther from the train-
 366 ing paradigm than S_{diff} or on-axis $S_{\text{diff}+}$. Whilst this suggests that caution must be used when in-
 367 terpreting denoised data that is outside of the training regime, that Figure 5a and 5b are so similar
 368 provides reassurance that the DAE can elucidate signals that it has not been specifically trained to
 369 extract, and motivates application to real $S_{\text{diff}+}$ data.

370 3.3 Application to real signals

371 Following the positive results of the synthetic tests, we apply the DAE to real $S_{\text{diff}+}$ waveforms.
 372 In the example shown in Figure 6, we apply a DAE to Event 20131123 (see Supplementary Section

373 S1 for details of all events referenced in this paper) recorded in the contiguous US that samples a ULVZ
 374 in the central Pacific (Martin et al., 2024). This DAE is trained on GSN noise, so has not seen the
 375 noise from any of the stations in the test data, and is trained on synthetic Instaseis signal, so has never
 376 seen real seismic waveforms. The synthetics used to train this particular DAE were filtered at 2 - 100 s,
 377 so the real traces are filtered to 2 - 100 s prior to denoising and are then filtered to the narrower pe-
 378 riod bands after denoising.

379 Figure 6 shows the original and denoised traces, and signal is extracted across all period bands.
 380 $S_{\text{diff}+}$ is clearly extracted in the 6.8 - 13.6 s and 4.5 - 9.0 s period bands but is weaker off-axis, as in
 381 the synthetic testing. $S_{\text{diff}+}$ is absent or weak in the extracted 3.0 - 6.0 s and 2.0 - 4.0 s period bands
 382 – this could also be mirroring the trend observed in the synthetic testing of poorer performance at
 383 higher noise levels, or could be a genuine lack of high-frequency $S_{\text{diff}+}$ from this ULVZ (Martin et al.,
 384 2024). Unlike in synthetic testing where a ground truth is known, it is not possible to know for real
 385 data. As is apparent from the difference between the top and bottom rows in Figure 6, there is al-
 386 ways some amplitude loss due to non-perfect partitioning of signal and noise (Zhu et al., 2019) – this
 387 is consistent with the synthetics tests. These results show the promise of the DAE in extracting real
 388 teleseismic signal, including exposing signal that is barely visible in the original data, despite being
 389 trained on purely synthetic arrivals.

390 3.4 Specificity of the noise

391 Different locations on Earth’s surface experience different seismic noise regimes. The aim of us-
 392 ing the DAE in this study is primarily to suppress the microseism, which is globally pervasive in the
 393 period bands in which we wish to study ULVZs. In order to test how the DAE trained with noise from
 394 the GSN performs in different locations, we build three localised noise datasets: one each for the con-
 395 tiguous US (using network codes TA and US), Alaska (using network codes AK and AV), and Japan
 396 (using F-net stations). These are varied locations – the US is largely a continental environment, Alaska
 397 is a high-latitude environment, and Japan is an island. For each dataset we download 128,000 noise
 398 traces and we retrain a DAE that was originally trained with GSN noise.

399 We apply each retrained DAE to events recorded in each of these regions and assess their per-
 400 formance. The aim is to test how well local noise conditions are suppressed by a DAE trained on global
 401 noise, and to see if retraining to local noise conditions improves on this. We define SNR in decibels
 402 (e.g. Zhu et al., 2019; Heuel & Friederich, 2022) as

$$403 \text{SNR} = 20 \log_{10} \left(\frac{\text{RMS}_{\text{signal}}}{\text{RMS}_{\text{noise}}} \right) \quad (11)$$

404 where $\text{RMS}_{\text{signal}}$ is the RMS amplitude of a 40 s long time window extending from the S_{diff} arrival
 405 time, t_0 , to t_0+40 s, and $\text{RMS}_{\text{noise}}$ is the RMS amplitude of a 40 s long time window from t_0-70 s
 406 to t_0-30 s. We also define the improvement in SNR, ΔSNR , as

$$407 \Delta\text{SNR} = \text{SNR}_{\text{denoised}} - \text{SNR}_{\text{original}}. \quad (12)$$

408 Figure 7 shows ΔSNR for each DAE for three events. The waveforms are filtered at 2.0 - 100 s
 409 to encompass noise suppression across the entire valid period range. In each region the DAE that achieves
 410 the best ΔSNR is typically the one retrained with noise from that region, but the improvements over
 411 the GSN DAE are marginal. In addition, retraining with noise from a different region usually reduces
 412 performance compared to the GSN DAE, although this is marginal. Furthermore, the waveforms them-
 413 selves look highly similar (Supplementary Section S6).

414 These results suggest that the predominant local noise conditions in these three locations are
 well-represented in the GSN training data and correspondingly suppressed by the DAE; this is expected
 as the microseism is the main noise source affecting these data. We therefore suggest that the DAE

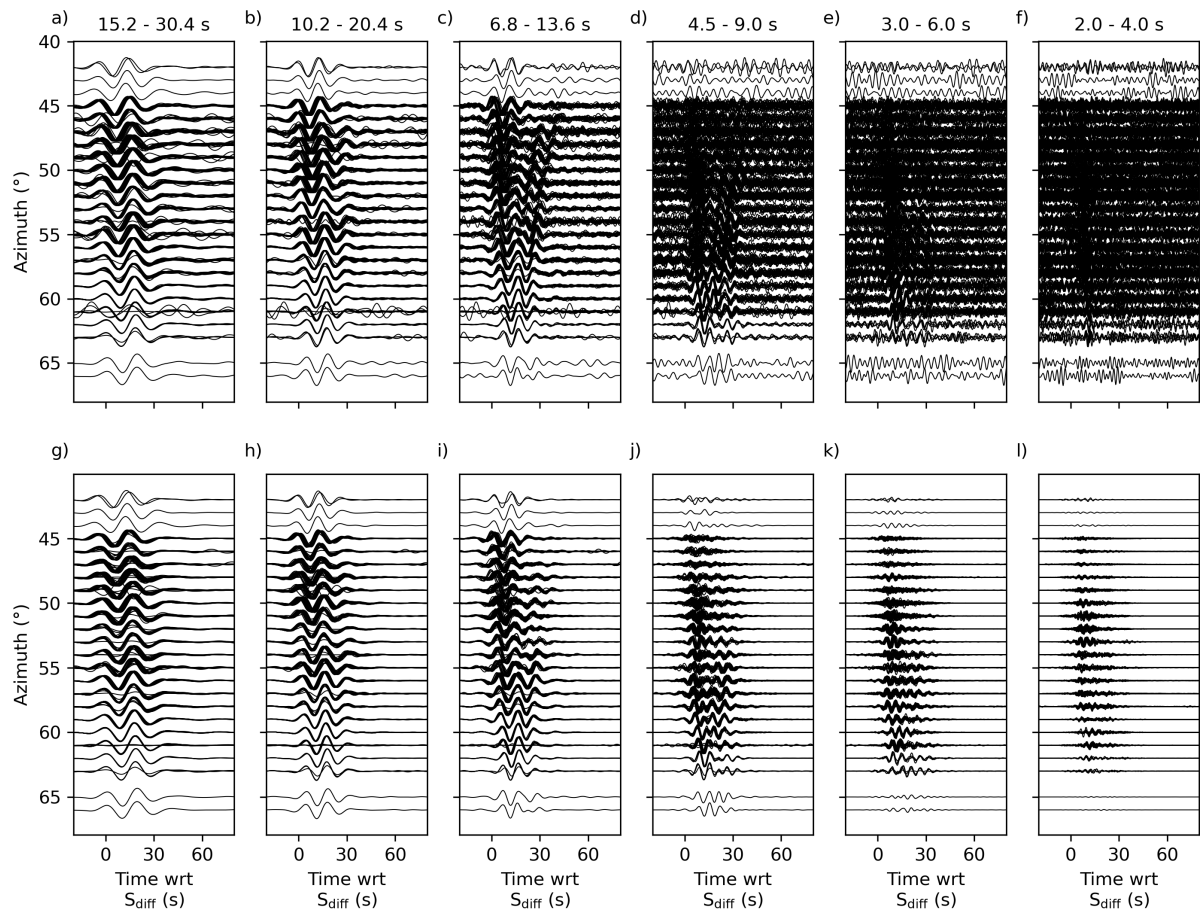


Figure 6. Example denoised waveforms for Event 20131123 recorded in the contiguous US in six different octave-width filter-bands. a) - e) Original waveforms in the period bands indicated. In the top row, traces are individually normalised such that the maximum amplitude corresponds to 0.75° azimuth, and traces are plotted rounded to the nearest degree of azimuth. f) - j) Denoised waveforms in the period bands indicated above each plot. The amplitudes in panels f) - j) are consistent with corresponding waveforms in panels a) - e).

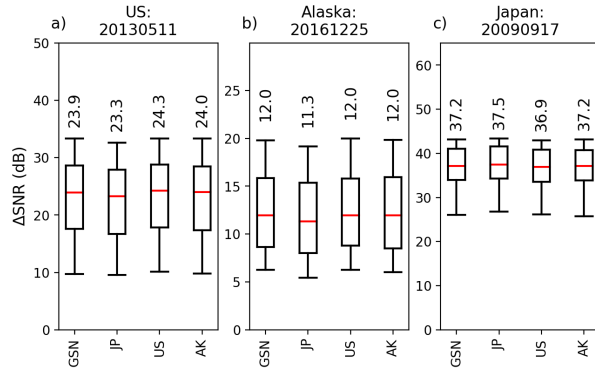


Figure 7. The performance of retrained DAE models on data recorded in different regions. a) The improvement in SNR in decibels for Event 20130511 recorded in the contiguous US, b) for Event 20161225 recorded in Alaska, and c) for Event 20240223 recorded in Japan. The median is shown in red, the edges of the boxes are the 25th and 75th percentile, and the ends of the arms are the 10th and 90th percentile. The value of the median is given above.

415 trained with GSN noise likely performs well globally. Nonetheless, for individual stations with highly
 416 specific noise regimes, for example those close to anthropogenic noise sources such as wind farms, high-
 417 ways, or deployed in urban environments, retraining with local noise may still be necessary to max-
 418 imise noise suppression. In this fashion, a single DAE trained with GSN noise could be used for screen-
 419 ing globally, but for more detailed down-stream analyses a retrained DAE could be implemented once
 420 a target set of signals is identified.

421 3.5 Specificity of the synthetics

422 As has been shown in the synthetic testing, $S_{\text{diff}+}$ can be suppressed by the Instaseis-trained DAE,
 423 even in the absence of noise. We therefore investigate whether retraining the DAE with AxiSEM3D
 424 synthetics that contain $S_{\text{diff}+}$ arrivals leads to better extraction of $S_{\text{diff}+}$ in real data. Figure 8 shows
 425 a DAE that has been retrained on AxiSEM3D synthetics applied to Event 20121207, recorded in the
 426 contiguous US, in the 6.8 - 13.6 s filter-band. This event has clear $S_{\text{diff}+}$ arrivals caused by the Pit-
 427 cairn ULVZ (Z. Li et al., 2024). Whilst the denoised waveforms for all models are a clear improve-
 428 ment over the original data, all models show a decrease in the ratio of the RMS amplitude of $S_{\text{diff}+}$
 429 to that of S_{diff} relative to the original data (panel e), measured in a 30 s window around each phase,
 430 from 65° to 75°. Consistent with expectations, this indicates that all of the DAEWs better extract S_{diff}
 431 than they do $S_{\text{diff}+}$.

432 The degradation of $S_{\text{diff}+}$ is somewhat remedied by retraining the DAE with AxiSEM3D syn-
 433 thetics that contain synthetic $S_{\text{diff}+}$ arrivals, which result in higher $S_{\text{diff}+}/S_{\text{diff}}$ ratios. $S_{\text{diff}+}$ extrac-
 434 tion is further improved by retraining with synthetics that are filtered to the 6.8 - 13.6 s filter-band.
 435 It is important to note that both of these models also have a slightly lower improvement in SNR for
 436 S_{diff} (panel f) compared to the Instaseis-trained DAE, indicating that they are less effective at sep-
 437 arating S_{diff} from noise, although due to the logarithmic definition of SNR the visual difference be-
 438 tween the waveforms is not substantial.

439 That panels b, c and d are so visually similar indicates that the Instaseis-trained DAE already
 440 performs well. However, these results show that further specification during training can lead to bet-
 441 ter extraction. These results also reiterate the danger of interpreting relative amplitudes in denoised
 442 data, as not all phases may be extracted equally. The outcomes of retraining with 3D synthetics are
 443 variable and does not always improve the extraction of $S_{\text{diff}+}$ (see Supplementary Section S7), which

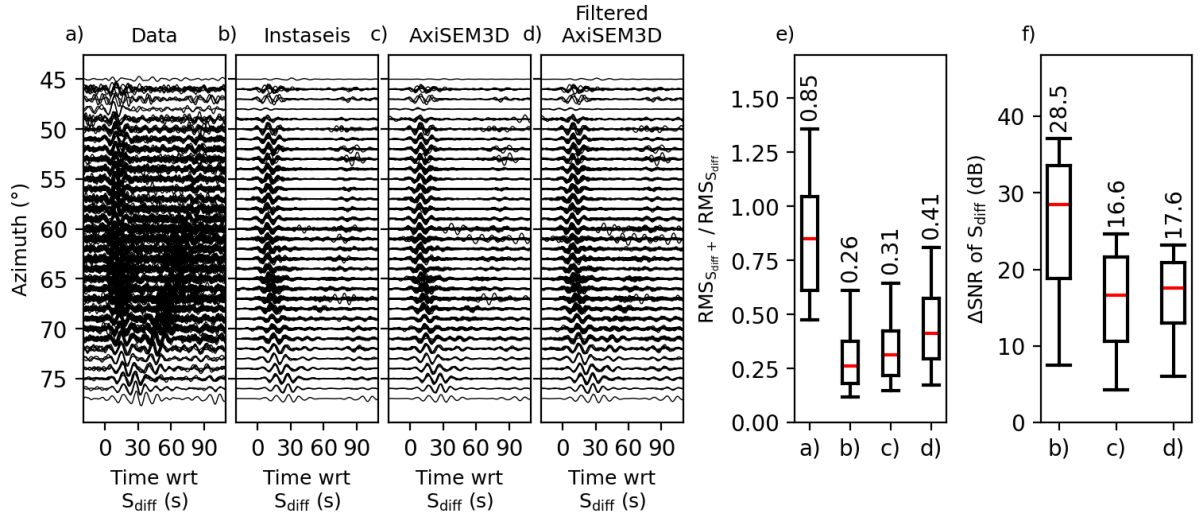


Figure 8. The performance of the DAE when retrained using AxiSEM3D synthetics applied to waveforms from Event 20121207 in the 6.8 - 13.6 s filter-band. a) The original data with each trace individually normalised such that the maximum amplitude corresponds to 0.75° azimuth, and traces are plotted rounded to the nearest degree of azimuth, b) denoised with the DAE trained with Instaseis synthetics, c) denoised with the DAE retrained with AxiSEM3D synthetics, and d) denoised with the DAE retrained with filtered AxiSEM3D synthetics. e) The ratios of the RMS of $S_{\text{diff}+}$ and S_{diff} for the waveforms in panels a) - d). The median is shown in red, the edges of the boxes are the 25th and 75th percentile, and the ends of the arms are the 10th and 90th percentile. The value of the median is given above. f) As for e) but showing the improvement in SNR for S_{diff} in decibels for panels b) - d) relative to a). Amplitudes in panels b) - d) are consistent with panel a).

444 is likely because the AxiSEM3D synthetics are too specific. Due to the computational cost involved,
 445 we only run one AxiSEM3D simulation with a single ULVZ that has only one combination of height,
 446 radius, S-velocity reduction, and a fixed source depth, parameters which may not be similar enough
 447 to an individual ULVZ to improve extraction. Generating a large dataset of ULVZ synthetics for a
 448 wide range of source and ULVZ parameters would be computationally extremely costly, but would be
 449 necessary for training a DAE that maximally extracts all $S_{\text{diff}+}$ signals.

450 3.6 Incorporating real training data

451 The final training datasets that we test incorporate real data. We retrain a DAE that was trained
 452 using the GSN and Instaseis synthetics using two different datasets of real data filtered to the 10.2 -
 453 20.4 s filter band: both tapered and non-tapered. Figure 9 shows these models applied to Event 20150519
 454 recorded in Japan, which has $S_{\text{diff}+}$ arrivals associated with the Vanuatu ULVZ (Martin et al., 2025).
 455 The real data used during retraining are recorded in the contiguous US, and therefore these data from
 456 Japan do not form part of the training dataset. All models have an improvement in SNR over the origi-
 457 nal data, but this is highest for the DAE retrained using tapered data. The DAE retrained with the
 458 untapered data sees only a minor improvement in SNR, although due to the logarithmic definition
 459 of SNR the visual improvement of the waveforms over the original is still significant. This demonstrates
 460 the insidious consequences of noise contamination in the training signals, which leads to the retrained
 461 DAE not performing as well as the original Instaseis DAE.

462 These results suggest that performance can be improved by incorporating real data even when
 463 applied to unseen data, but for best results one must be careful to isolate the signal as best as pos-

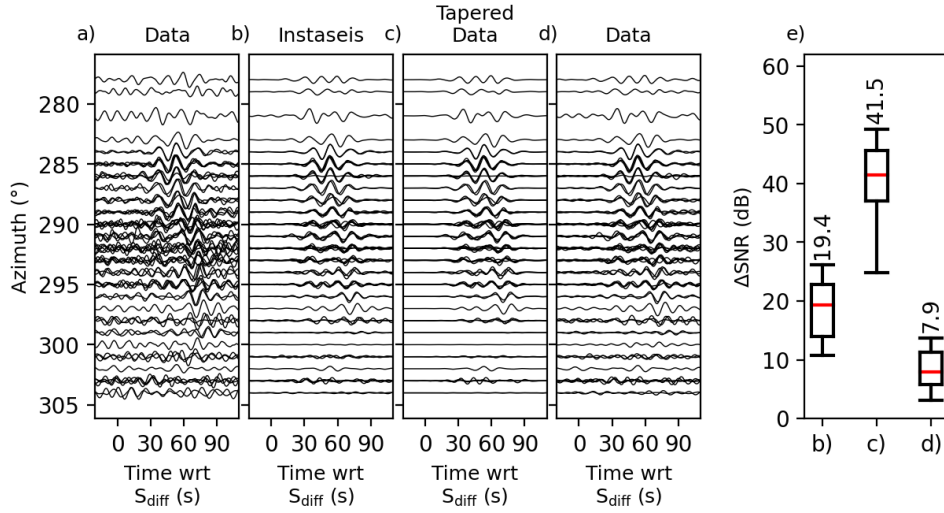


Figure 9. The performance of the DAE when retrained with real data, applied to Event 20150519 recorded in Japan in the filter-band 10.2 - 20.4 s. a) The original data with each trace individually normalised such that the maximum amplitude corresponds to 0.75° azimuth, and traces are plotted rounded to the nearest degree of azimuth, b) denoised with the DAE trained with Instaseis synthetics filtered 10.2 - 20.4 s, c) denoised with the DAE retrained with real data that has been tapered and filtered 10.2 - 20.4 s, and d) denoised with real data that has been filtered 10.2 - 20.4 s. e) The improvement in SNR for for the waveforms in panels b) - d) relative to a). The median is shown in red, the edges of the boxes are the 25th and 75th percentile, and the ends of the arms are the 10th and 90th percentile. The value of the median is given above. Amplitudes in panels b) - d) are consistent with panel a). Note that as the waveforms are severely delayed due to the Pacific LLSVP, the 40 s long time window used for the S_{diff} RMS starts at 30 s after the theoretical S_{diff} arrival time. The time window for the noise is unchanged.

464 sible to avoid noise contamination. Constructing training datasets of specific low-amplitude signals
 465 where noise levels are typically high may not be possible, and therefore this strategy may not help for
 466 extracting data that is most affected by noise. Real data are best incorporated during a second training
 467 stage due to the generally small number of waveforms available for high-quality training datasets,
 468 allowing the bulk of the learning to be done on synthetics prior to retraining.

469 3.7 Stacking as a companion to denoising

470 The most commonly used method in deep Earth seismology to improve SNR, after spectral fil-
 471 tering, is stacking (see Rost & Thomas, 2002, for a comprehensive overview of array methods includ-
 472 ing stacking). Where there are several seismic stations in a region, known as an array, it is possible
 473 to spatially average the signals from these stations (Rost & Thomas, 2002, 2009; Schweitzer et al., 2012).
 474 Arrays may be deployed specifically for this purpose, or be created ad-hoc by grouping nearby sta-
 475 tions together. By making an assumption about the directionality of the incoming energy, usually that
 476 it is a plane wave with specified slowness and back-azimuth, one can correct for the travel time dif-
 477 ference between stations, a process known as beamforming, and then average the shifted seismic traces
 478 in the time domain. This leads to the suppression of incoherent energy (i.e. noise) and the ampli-
 479 fication of coherent energy (i.e. the incoming teleseismic plane wave). Stacking functions as a slowness-
 480 back-azimuth filter, allowing the extraction of signal in the same period band as pervasive noise, pro-
 481 vided the directional properties of the signal and noise differ.

482 There are a plethora of different averaging methods of varying complexity that can be imple-
 483 mented following beamforming. Examples include linear stacking (Davies et al., 1971), n^{th} -root stack-
 484 ing (Kanasewich et al., 1973), phase-weighted stacking (Schimmel & Paulssen, 1997), F-trace stack-
 485 ing (Blandford, 1974), and iterative stacking schemes (Hansen et al., 2021). Each method of stack-
 486 ing has its own advantages and disadvantages, including varying efficacy of noise suppression, wave-
 487 form distortion and amplitude fidelity. Linear stacking is conceptually the easiest to implement, most
 488 commonly used, and has the advantage that it preserves waveform timing, shape and amplitude (Rost
 489 & Thomas, 2002).

490 The slowness and back-azimuth of the target signal must be known in order to stack optimally,
 491 otherwise coherent signals with differing directional properties will be suppressed; for example in our
 492 application, stacking for S_{diff} would suppress $S_{\text{diff}+}$ as it arrives from a different direction. For anomalous
 493 signals, the directional information may not be known in advance, and so one can iterate through
 494 different slowness and back-azimuth values, taking the highest amplitude stack as the truth. This is
 495 a slow iterative process but can identify the direction and slowness of incoming signal. It is by this
 496 method that ULVZs can be located from the direction of the post-cursory energy (e.g. Cottaar & Ro-
 497 manowicz, 2012; Martin et al., 2023b; Jagt et al., 2024).

498 Here, we test how the DAE performs relative to linear stacking, and also demonstrate stacking
 499 as a useful companion to denoising. We also verify that the directions recovered from beamforming
 500 $S_{\text{diff}+}$ waveforms are consistent in both original and denoised waveforms. We use waveforms from Event
 501 20100320 recorded in the contiguous US, which have high-amplitude post-cursors generated by the
 502 Hawaiian ULVZ; the post-cursors of this event have been well-examined by previous studies (Cottaar
 503 & Romanowicz, 2012; Lai et al., 2022; Z. Li et al., 2022; J. Li et al., 2022; Martin et al., 2023a; Jagt
 504 et al., 2024). For every station we linearly stack all stations within a 2° (~ 220 km) radius. As both
 505 S_{diff} and $S_{\text{diff}+}$ diffract along the CMB, we fix the stacking slowness to $8.36^\circ/\text{s}$, which is the critical
 506 slowness for the CMB in PREM. As S_{diff} and $S_{\text{diff}+}$ arrive from different directions, we create stacks
 507 separately for each phase; for S_{diff} we fix the back-azimuth to the great circle path, and for $S_{\text{diff}+}$ we
 508 allow back-azimuth to vary from -25° to 0° relative to the great circle path in 1° intervals, taking the
 509 stack with the highest amplitude.

510 We use a DAE that has been retrained to Instaseis synthetics filtered to the specific period band,
 511 and results for the 10.2 - 20.4 s and 3.0 - 6.0 s filter-bands are shown in Figure 10, the former filter-
 512 band being close to that used by Cottaar & Romanowicz (2012) and the latter to that used by Z. Li
 513 et al. (2022). In panel a, the standard post-cursor delayed by 20 - 40 s is visible, and in panel g the
 514 short-period post-cursor delayed by 40 - 80 s is visible. In both filter-bands, both stacking and denois-
 515 ing increase the SNR and improve the visibility of the $S_{\text{diff}+}$, but the best results are achieved when
 516 both techniques are used together by stacking the denoised data.

517 The back-azimuths measured from the original and denoised data are consistent, demonstrat-
 518 ing that array methods can be applied effectively to denoised data while preserving the directional
 519 information. Furthermore, as is apparent in the 3.0 - 6.0 s filter-band, comparing panels i and j, stack-
 520 ing can help to suppress ringing and erroneous signal present in the denoised data. These results sug-
 521 gest that combining these two complimentary techniques can lead to more effective noise suppression
 522 than each technique used in isolation.

523 4 Example applications to known ULVZs

524 4.1 Short-period signals

525 The short-period post-cursor used by Z. Li et al. (2022) to infer a greater velocity reduction at
 526 the base of the Hawaiian ULVZ is a consistent and coherent feature in the short-period denoised data
 527 shown in Figure 10 panels g - j, giving confidence that this is a robust signal. We highlight two fur-
 528 ther signals that are especially apparent in the denoised waveforms in panel j: there is a high frequency
 529 pre-cursor, marked in purple, and a second signal between S_{diff} and $S_{\text{diff}+}$, marked in red. Both of these
 530 signals have similar move-out to the post-cursors, i.e. arriving out of plane, indicating that they orig-

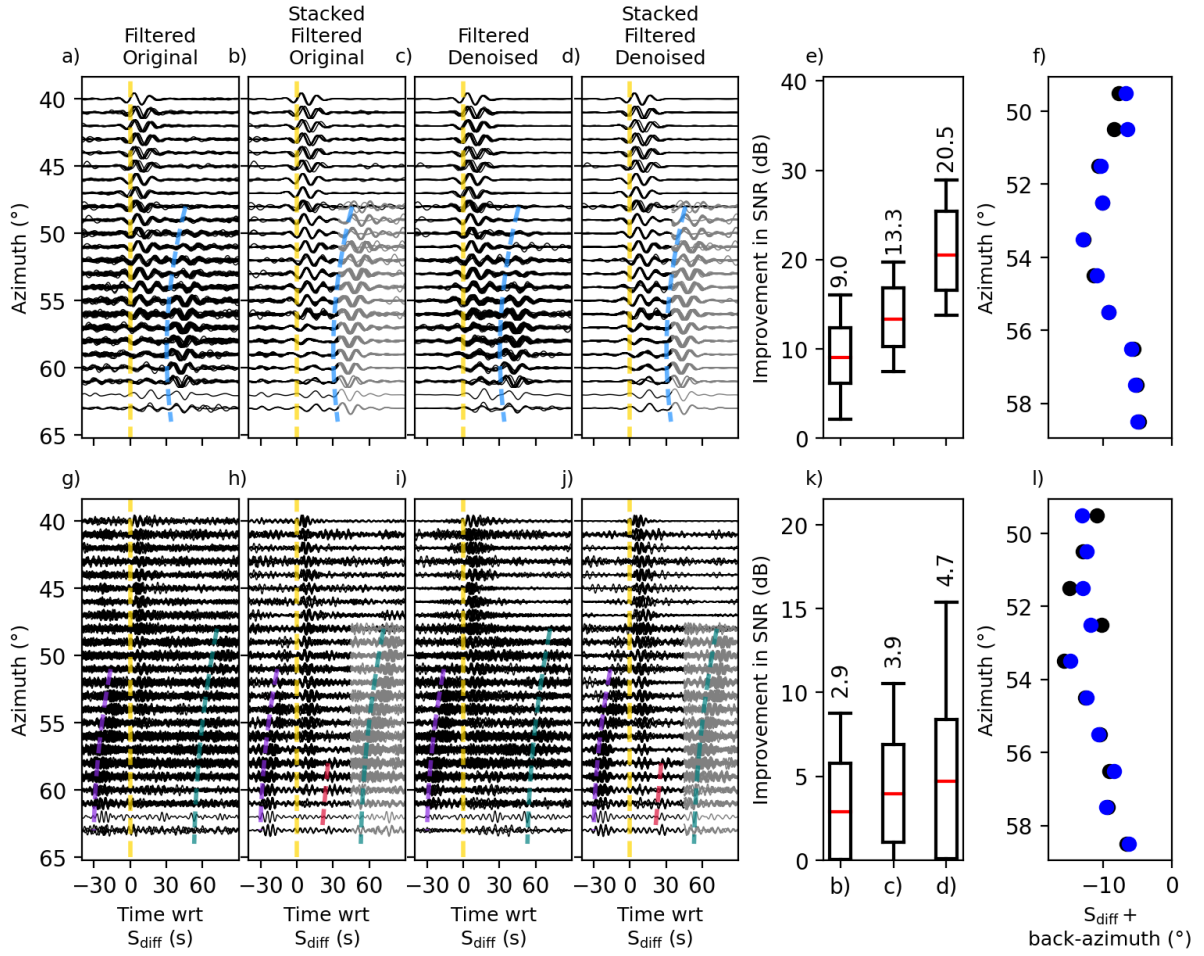


Figure 10. Comparison of the DAE with stacking for Event 20100320 recorded in the contiguous US filtered 10.2 - 20.4 s (top row) and 3.0 - 6.0 s (bottom row). a) The original data, b) the stacked data – the separate stacks for $S_{\text{diff}+}$ are shown in grey where calculated, c) the denoised data, d) the stacked denoised data. Traces and stacks in panels a) - d) are individually normalised such that the maximum amplitude corresponds to 0.5° azimuth, and are plotted rounded to the nearest degree of azimuth. Coherent signals are marked as dashed coloured lines to guide the eye, including the 10 - 20 s $S_{\text{diff}+}$ (Cottaar & Romanowicz, 2012) in blue and the short-period $S_{\text{diff}+}$ (Z. Li et al., 2022) in teal. e) The improvement in SNR for the waveforms in panels b) - d) relative to a). The median is shown in red, the edges of the boxes are the 25th and 75th percentile, and the ends of the arms are the 10th and 90th percentile. The value of the median is given above. f) The mean recovered back-azimuths of the greatest amplitude stacks for $S_{\text{diff}+}$ in 1° azimuth bins, for the original (black) and denoised (blue) data. Panels g) - l) are as for a) - f) but filtered at 3.0 - 6.0 s.

531 inate from 3D structure, likely the ULVZ. To the best of our knowledge, neither of these signals has
532 been identified by previous studies of ULVZs, but are clear and coherent when denoising and stack-
533 ing are applied.

534 We apply this method of denoising and stacking to several events that sample known ULVZs.
535 For two events, 2010080407 and 20100417, that sample the Hawaiian ULVZ and for two further events,
536 20161225 and 20121207, that sample the Galápagos and Pitcairn ULVZs, respectively. The resulting
537 resulting waveforms are shown in Figure 11. Both events that sample the Hawaiian ULVZ show clear
538 pre-cursors, while those that sample the Galápagos and Pitcairn ULVZs also show possible pre-cursors.
539 Some of these signals are still poor quality and correspondingly are marked with question marks to
540 denote the uncertainty.

541 In many of these examples, the short-period signals are not visible in the original or stacked data,
542 showing that denoising can make a material difference for identifying low-amplitude high-frequency
543 signals from ULVZs. The cause of these out-of-plane signals – which have not been identified in the
544 literature – is still unknown, but we suggest the the precursor, as a feature across several events, is
545 likely scattered energy related to the ULVZ or nearby structure. These signals warrant further inves-
546 tigation.

547 4.2 Signals of the Hawaiian ULVZ recorded in Japan

548 The Hawaiian ULVZ is the most studied ULVZ, as well as the largest, but there is still much that
549 is unknown. In particular, the shape of the ULVZ, which is usually assumed to be cylindrical for mod-
550 elling purposes, remains poorly constrained. In large part this is due to the over-reliance on source-
551 receiver geometries from the south-western Pacific, where there are many earthquakes, to North Amer-
552 ica, where there are many seismometers. Due to trade-offs along the S_{diff} diffracted path, it is not pos-
553 sible to uniquely constrain the size and shape of a ULVZ from unidirectional S_{diff} observations, and
554 almost all previous literature using S_{diff} has focussed on this geometry (Cottaar & Romanowicz, 2012;
555 Lai et al., 2022; Z. Li et al., 2022; J. Li et al., 2022; Martin et al., 2023a).

556 Martin et al. (2023a) compiled a dataset of almost 100 events that sample the Hawaiian ULVZ,
557 providing unprecedented data coverage. They also noted the possible source-receiver geometry from
558 events on the southern East Pacific Rise to Japan – where there is a large network of broadband seis-
559 mometers, F-net (Okada et al., 2004) – but did not unambiguously identify $S_{\text{diff}+}$ signals from these
560 events. A single event, 20090917, was marked as possibly containing $S_{\text{diff}+}$, but the low data qual-
561 ity precluded certainty. No data was found from stations in Japan that could be used to provide a com-
562 plimentary dataset to $S_{\text{diff}+}$ recorded in North America. A recent global compilation of $S_{\text{diff}+}$ also
563 contained no observations of the Hawaiian ULVZ from stations in Japan (Atkins et al., 2026).

564 As a final application, we apply a DAE to S_{diff} record sections recorded on F-net seismometers
565 in Japan originating from earthquakes on the East Pacific Rise. To maximise possible detection we
566 use a DAE that is originally trained on GSN noise and Instaseis synthetics, that has been retrained
567 with real tapered S_{diff} recorded in North America. We examine the signals a function effective azimuth,
568 defined as the difference between the source-to-ULVZ azimuth, and the ULVZ-to-station azimuth; ef-
569 fective azimuth is therefore a measure of expected refraction angle with respect to the ULVZ (Mar-
570 tin et al., 2023a). If the location of the ULVZ is correct, the $S_{\text{diff}+}$ signals are symmetric about 0° ef-
571 fective azimuth; we use the preferred centre location of Z. Li et al. (2022), 15.4°N and 172.3°W .

572 Using our DAE-assisted workflow, we identify four events containing $S_{\text{diff}+}$ signals (Figure 12).
573 These post-cursors are different in character to those caused by the Hawaiian ULVZ as recorded in
574 North America. The move-out parabolas are shallower, and $S_{\text{diff}+}$ is not well separated from the main
575 S_{diff} . These $S_{\text{diff}+}$ arrivals are, however, visible over a relatively wide azimuthal range. We note that,
576 judging by eye, the centre of the parabola typically centres between -5° and -10° effective azimuth,
577 indicating that the best-fitting ULVZ location for the data in North America does not well-fit the data
578 in Japan. Our new observations appear to be consistent with a more south-westerly location and el-
579 liptical structure, as suggested by Martin et al. (2023a).

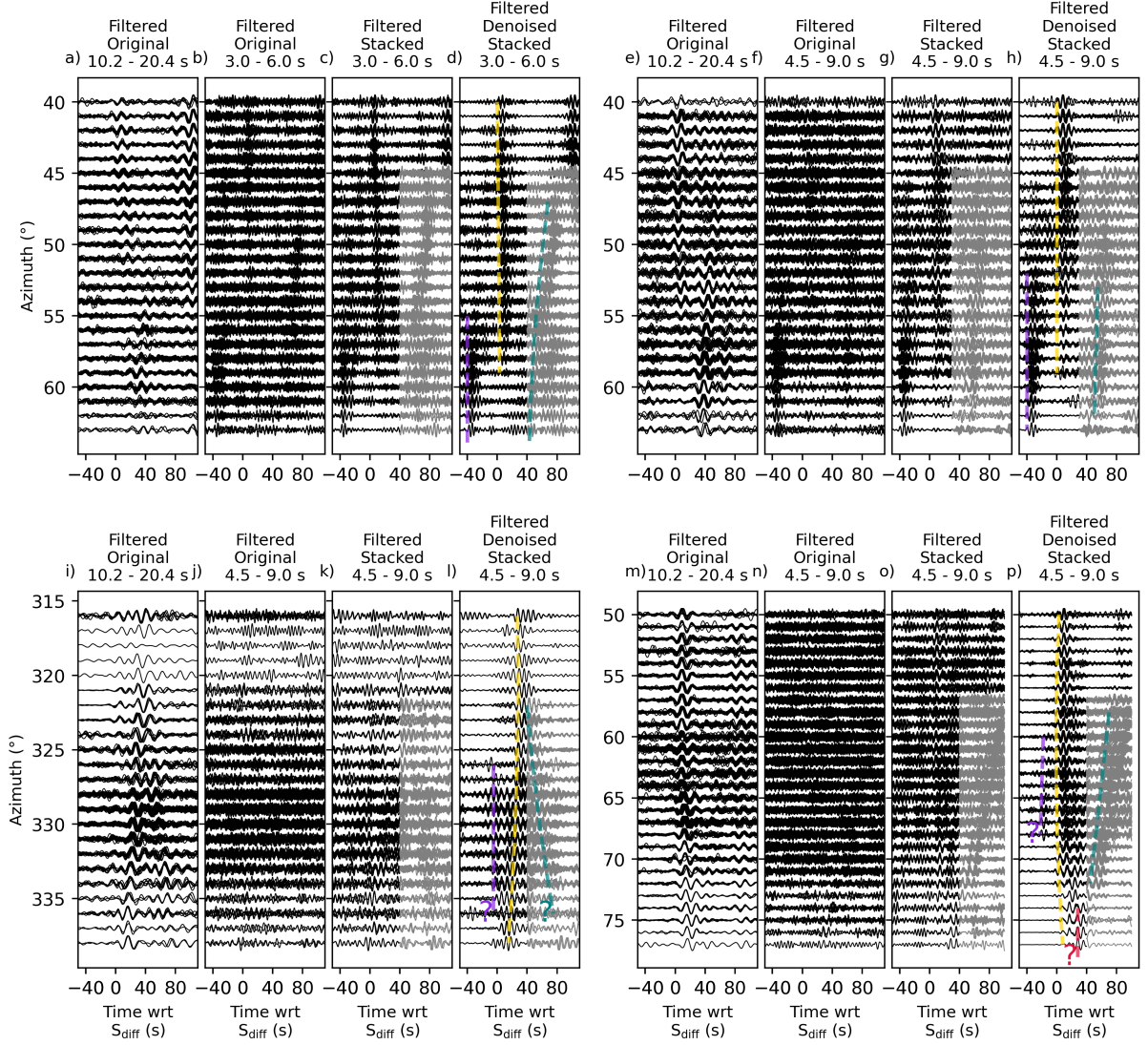


Figure 11. Examples of short-period signals elucidated by the DAE. Event 20100804 sampling the Hawaiian ULVZ filtered 3.0 - 6.0 s (panels a - d), Event 20100417 sampling the Hawaiian ULVZ filtered 4.5 - 9.0 s (panels e - h), Event 20161225 sampling the Galápagos ULVZ filtered 3.0 - 6.0 s (panels i - l), and Event 20121207 sampling the Pitcairn ULVZ filtered 2.0 - 4.0 s (panels m - p). For all events the first column is the original data filtered at longer period, the second is the original data filtered at short period, the third is short-period stacked data, and the fourth is short-period stacked denoised data. Traces where $S_{\text{diff}+}$ is expected is stacked separately for this time window and plotted in grey. Coherent signals are marked in the third column where visible; tentative signals are marked with a question mark.

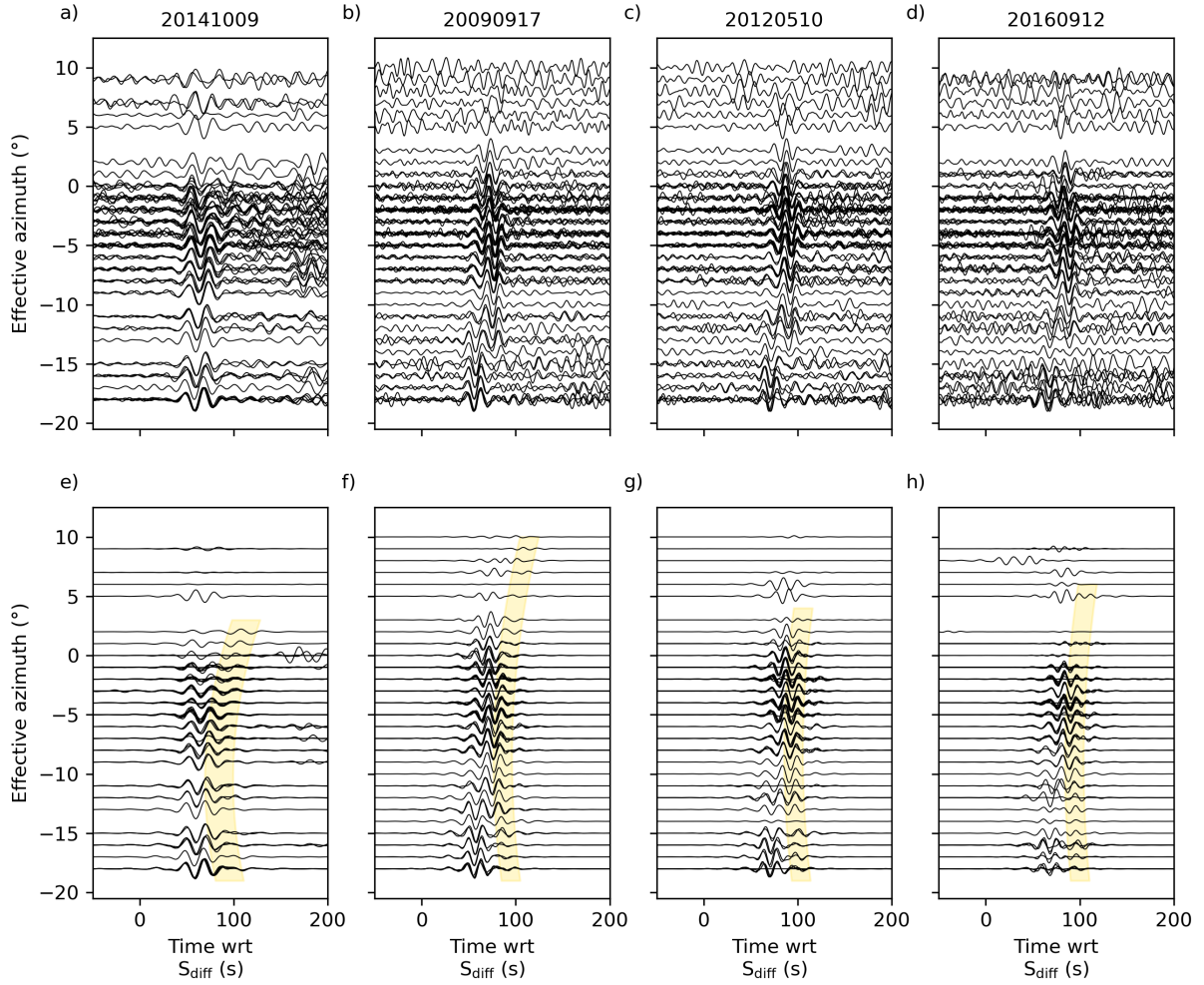


Figure 12. Examples of $S_{\text{diff}+}$ resulting from the Hawaiian ULVZ recorded by F-net station in Japan. a) - d) shows the filtered data normalised such that the maximum amplitude corresponds to 0.75° azimuth, and traces are plotted rounded to the nearest degree of azimuth. e) - h) shows the denoised data with amplitudes consistent with the top row. Potential post-cursors are highlighted in yellow to guide the eye. All panels are filtered at 10.2 - 20.4 s, except for panels a) and e), which are filtered at 15.2 - 30.5 s. The significant time delay of these arrivals relative to PREM is due to the Pacific LLVP.

580 Some of these $S_{\text{diff}+}$ signals are visible in the original data, but are difficult to identify due to
581 the high noise level in Japan. Denoising highlights these signals and demonstrates its utility to deep
582 Earth studies. These signals require further investigation to ascertain exactly why the manifestation
583 of the Hawaiian ULVZ in Japan is so different to in North America.

584 5 Discussion

585 5.1 Reliability of the DAE

586 There are several points about the workflow that give us high confidence in the signals extracted
587 by the DAE: (1) Traces are denoised one-at-a-time and the DAE has no spatial or temporal knowl-
588 edge of the stations or traces. This means that it is not possible for the DAE to introduce coherent
589 signal between traces unless there is coherent energy already present in those traces. While there may
590 be uncertainty in any particular signal extracted in a single trace, there is high confidence in signals
591 that are coherent across stations as a function of distance and/or azimuth, even when they are low
592 amplitude, as they have been extracted independently. (2) The mask functions have values between
593 0 and 1, and so any particular point in the resulting time-frequency images can only be as high in am-
594 plitude as the same point in the original time-frequency representation. In other words, seismic en-
595 ergy cannot be created where it does not already exist. This does not mean that all extracted signal
596 is correct. For instance, erroneous extracted signals are apparent in some of the figures shown in this
597 paper, but these are typically low amplitude and are always incoherent across the record sections. Stack-
598 ing the denoised traces provides an effective and complementary way of suppressing these incoherent
599 erroneous signals. (3) As the same mask functions are applied to both the real and imaginary parts
600 of the STFT, there is no phase shift introduced between the input and output traces. The potential
601 for waveform distortion is therefore minimal and important time-axis observables, such as the arrival
602 times of seismic phases, are well-preserved.

603 There are, of course, still warnings and caveats that must be considered when using the DAE.
604 Most importantly, as we have noted, amplitude fidelity is a major limitation and amplitude loss may
605 not be consistent across a trace or set of arrivals. Making amplitude measurements, even relative ones,
606 on denoised traces is therefore to be discouraged. Despite the significant advantages of using mask
607 functions outlined above, the mask functions themselves are a source of imperfect partitioning of sig-
608 nal and noise, as noted by previous studies (Zhu et al., 2019; Heuel & Friederich, 2022). It is possi-
609 ble for seismic energy to be incorrectly partitioned and for signals to be missed entirely, especially where
610 the application data are unlike the training data. A lack of extracted signal should not be taken as
611 a true lack of signal, simply a lack of signal that is similar enough to the training data to be extracted.
612 We suggest retraining with more representative signals if this is suspected.

613 Finally, we note that the DAE is best at identifying signals when the noise level is already low
614 – this is unsurprising as clearly clean signals are more trivial to identify, even for a deep learning al-
615 gorithm. In cases where the initial noise level is low, all metrics including amplitudes and times are
616 better preserved and these degrade as the initial noise level increases. Whilst the DAE is therefore
617 expected to perform better at ‘tidying up’ signal that is only partly obscured by noise, our results clearly
618 demonstrate that it is also successful at revealing hidden signals that are completely obscured by noise.
619 For screening purposes, where the aim is to elucidate the possible presence of signal, the DAE would
620 be highly appropriate in spite of sub-optimal extraction at high noise levels.

621 5.2 Potential deep Earth use cases

622 We have used S_{diff} and its ULVZ-generated post-cursor, $S_{\text{diff}+}$, as a case study to demonstrate
623 the effectiveness and potential of the DAE in improving data quality for deep Earth body wave stud-
624 ies. The benefits to denoising these phases are readily apparent in helping to better understand UL-
625 VZs, for which many important properties remain poorly constrained. There are a wide array of other
626 possible applications of deep-learning based denoising in deep Earth seismology, although due to the
627 loss of amplitudes, which may not be consistent between phases, the DAE would not be appropriate

628 for studies that intend to use amplitudes. We envision the DAE being most useful for the initial screen-
629 ing and identification of seismic phases that can then be the subject of further detailed investigation.

630 The DAE has proven particularly effective at removing ocean-generated microseism and so would
631 be expected to be useful for stations with high oceanic noise levels such as the Caribbean, ocean is-
632 lands, or OBS deployments, where teleseismic observations are challenging – as demonstrated by strong
633 performance on data from Japan. Furthermore, by transfer learning, the DAE can be efficiently op-
634 timised for use in places with a unique noise environment such as Antarctica (Anthony et al., 2015),
635 a region that is increasingly being used for deep Earth seismic research (e.g. Brett & Deuss, 2020; Hansen
636 et al., 2023).

637 Increasing global data coverage in this manner is highly desirable. For the ULVZs that have been
638 the focus of this study, better global sampling could allow imaging of ULVZs from new directions, as
639 we have demonstrated using Japanese F-net data, allowing better constraints on size and morphol-
640 ogy, as well as the discovery of ULVZs in new locations. This would help to better map global dis-
641 tributions (e.g. Yu & Garnero, 2018; Thorne et al., 2021; Atkins et al., 2026). Many other deep Earth
642 applications suffer from geographic bias and, most notably, this has a major impact on tomographic
643 models (e.g. Foulger et al., 2013; Ruan et al., 2019). As the DAE preserves travel time information,
644 there is clear potential for the DAE to be used in the construction of tomographic models using phase-
645 based metrics.

646 The study of Earth’s inner core is another area where denoising may prove useful; since the in-
647 ner core is highly attenuating and body wave observations are often low amplitude (e.g. Cormier et
648 al., 2021), and adequate and representative data distribution is key (e.g. Frost et al., 2021; Waszek
649 et al., 2023). Constraining the magnitude and directionality of P-wave anisotropy is essential; in par-
650 ticular, further robust observations of polar geometries are required (e.g. Brett & Deuss, 2020), but
651 such measurements are often made from stations in noisy high-latitude environments with low sta-
652 tion density. The innermost inner core, a potentially distinct region at the very centre of the planet,
653 is the subject of intense research to unambiguously identify and constrain its properties (e.g. Lyth-
654 goe et al., 2014; Stephenson et al., 2021; Brett et al., 2022; Costa de Lima et al., 2022). This task would
655 be helped by observations of deeper-bottoming phases, which has been the subject of recent efforts
656 with machine learning (Zhou et al., 2024).

657 5.3 Possible future developments

658 Based on the criteria that we have set for downloading GSN noise, we have only used $\sim 0.12\%$
659 of the >70 million hours of available training noise. This is only for the GSN – incorporating other
660 networks could massively increase the available training noise again. The training synthetics are also
661 limited; for example, the Instaseis synthetics are an idealised and unrealistic signal prior. However,
662 creating a diverse training dataset of 3D synthetics, by incorporating ULVZs, tomographic or crustal
663 models, would involve significant computational cost. An alternative to running costly 3D simulations
664 is to convolve 1D synthetics with crustal responses (Zhou et al., 2024). Other S phases or P waves could
665 also be incorporated to diversify the training data. The potential to develop better performing mod-
666 els, based on more numerous and varied training data, is apparent, but performance scaling has not
667 been quantified.

668 The learning process could also be modified. At present, the classification of each point of the
669 input STFT into signal and noise is treated as a binary classification task and performance is mea-
670 sured by binary cross-entropy on the masks themselves. Implementing multi-resolution STFT inputs
671 or performance metrics may better characterise frequency content, allowing more effective discrim-
672 ination (e.g. Engel et al., 2020; Yamamoto et al., 2020). Reformulation into a regression task on the
673 masks or measuring performance on the traces in the time domain are alternative options. Outputting
674 signal and noise directly is another possibility, but this would forfeit the benefits of using mask func-
675 tions.

676 One could also modify the architecture of the DAE to incorporate array information. By inte-
677 grating temporo-spatial information, as stacking does, we hypothesise that even greater noise suppres-
678 sion and signal extraction could be achieved. But this potential advantage would come with a trade-
679 off: the present trace-by-trace denoising implementation provides an important safety check, which
680 would be forfeited if the DAE was able to extract spurious signal coherently.

681 While the denoisers already perform well in our examples, the models used in this study rep-
682 resent only an initial demonstration of the potential of denoising teleseismic data with supervised deep-
683 learning. Alternative learning objectives and model architectures remain to be investigated, and the
684 performance demonstrated in this paper represents a lower bound on the ability of the DAE for this
685 task.

686 **6 Conclusions and recommendations**

687 In this study, we have demonstrated the potential of the DAE for improving teleseismic data qual-
688 ity for studying the deep Earth. We have presented a computationally efficient workflow that utilises
689 only Instaseis synthetics and global seismic noise for training, that manages to extract ULVZ-associated
690 signals from real seismic data. We have shown that denoising outperforms traditional spectral filter-
691 ing and can be used successfully alongside stacking to elucidate signals from ULVZs. We have also
692 established that the noise from the GSN provides sufficient global noise exposure for the DAE to work
693 in the regions that we have tested without further optimisation, but that specification to particular
694 types of seismic signal can enhance extraction. Therefore, when seeking the extraction of highly spe-
695 cific seismic signals, retraining via transfer learning can boost performance, including utilising small
696 datasets of real data.

697 We have focussed on denoising record sections that have visibly coherent seismic signals between
698 them, which provides a practical check on the outputs of the DAE: extracted signals that are coher-
699 ent between stations can be more confidently interpreted as genuine signals. While denoising and in-
700 terpreting signals in single stations is possible, it forfeits this simple and effective check and we ad-
701 vise caution when doing so. Amplitude fidelity is a major limitation, and amplitude measurements,
702 even relative ones, should not be made on the outputs of the DAE, particularly where the applica-
703 tion is dissimilar to the training data. Conversely the extraction of travel times is typically robust.
704 Performance by all metrics is reduced at high noise levels, but the DAE shows remarkable aptitude
705 for elucidating signals that are completely obscured by noise.

706 We have applied denoising in two applications, revealing new short-period observations likely
707 related to ULVZs, and identifying the signal of the Hawaiian ULVZ using a novel source-receiver ge-
708 ometry from the East Pacific Rise to Japan. The results and applications suggest that denoising is
709 a powerful tool that can compliment existing methodologies for processing and visualising deep Earth
710 seismic data. The potential for denoising to impact deep Earth seismology is apparent, and we hope
711 that by highlighting its capability and providing clear steps and recommendations for implementa-
712 tion, we will encourage the use of denoising in future studies.

713 **Acknowledgements**

714 SR acknowledges funding from the Deutsche Forschungsgemeinschaft (DFG), grant number TH1530/16-
715 3. WE acknowledges funding from the German Federal Ministry of Research, Technology and Space
716 (BMFTR), ErUM-WAVE project 05D2022. This study has made use of the computing cluster PALMA
717 II of Universität Münster, subsidised by the DFG (INST 211/667-1). We would like to thank Mag-
718 gie Chen at the University of Oxford and Sanne Cottaar at the University of Cambridge for valuable
719 conversations relevant to this work.

Data Availability

All seismic data used in this study is freely available online, either through the National Research Institute for Earth Science and Disaster Resilience (NIED; <https://www.hinet.bosai.go.jp/>) for Japanese F-net waveform data, or the U.S. National Science Foundation’s Seismological Facility for the Advancement of Geoscience (NSF SAGE; <https://www.iris.edu/hq/>) for all other waveform data. Data are available for convenient download using Python by using the ObsPy <https://pypi.org/project/obspy/> and HinetPy <https://pypi.org/project/HinetPy/> packages. The codes for training data compilation, training, re-training and denoising used in this study are freely available in a public GitHub repository <https://github.com/StuartJRussell/DeepSeisDAE/> under a GNU General Public License. A DAE is also implemented in SeisBench <https://seisbench.readthedocs.io/en/stable/>.

Competing interests

The authors declare that there are no conflicts of interest for this manuscript.

References

- Anthony, R. E., Aster, R. C., Wiens, D., Nyblade, A., Anandakrishnan, S., Huerta, A., ... Rowe, C. (2015). The seismic noise environment of Antarctica. *Seismological Research Letters*, 86(1), 89–100. doi: 10.1785/0220140109
- Atkins, J. R., Martin, C., & Cottaar, S. (2026). Global presence and absence of ultra-low velocity zones as seen by Sdiff postcursors. *Journal of Geophysical Research: Solid Earth*, 131(4), e2025JB033171. doi: 10.1029/2025JB033171
- Beyreuther, M., Barsch, R., Krischer, L., Megies, T., Behr, Y., & Wassermann, J. (2010). ObsPy: A Python toolbox for seismology. *Seismological Research Letters*, 81(3), 530–533. doi: 10.1785/gssrl.81.3.530
- Blandford, R. (1974). An automatic event detector at the Tonto Forest seismic observatory. *Geophysics*, 39(5), 633–643. doi: 10.1190/1.1440453
- Bormann, P., & Wielandt, E. (2013). Seismic signals and noise. In *New manual of seismological observatory practice 2 (nmsop2)* (pp. 1–62). Deutsches GeoForschungsZentrum GFZ.
- Brett, H., & Deuss, A. (2020). Inner core anisotropy measured using new ultra-polar PKIKP paths. *Geophysical Journal International*, 223(2), 1230–1246. doi: 10.1093/gji/ggaa348
- Brett, H., Hawkins, R., Waszek, L., Lythgoe, K., & Deuss, A. (2022). 3D transdimensional seismic tomography of the inner core. *Earth and Planetary Science Letters*, 593, 117688. doi: 10.1016/j.epsl.2022.117688
- Bridle, J. S. (1990). Probabilistic interpretation of feedforward classification network outputs, with relationships to statistical pattern recognition. In *Neurocomputing: Algorithms, architectures and applications* (pp. 227–236). Springer. doi: 10.1007/978-3-642-76153-9_28
- Chaljub, E., Komatitsch, D., Vilotte, J.-P., Capdeville, Y., Valette, B., & Festa, G. (2007). Spectral-element analysis in seismology. *Advances in geophysics*, 48, 365–419. doi: 10.1016/S0065-2687(06)48007-9
- Cormier, V. F., Bergman, M. I., & Olson, P. L. (2021). *Earth’s core: Geophysics of a planet’s deepest interior*. Elsevier.
- Costa de Lima, T., Tkalčić, H., & Waszek, L. (2022). A new probe into the innermost inner core anisotropy via the global coda-correlation wavefield. *Journal of Geophysical Research: Solid Earth*, 127(4), e2021JB023540. doi: 10.1029/2021JB023540
- Cottaar, S., Martin, C., Li, Z., & Parai, R. (2022). The root to the Galápagos mantle plume on the core-mantle boundary. *Seismica*, 1(1), 197. doi: 10.26443/seismica.v1i1.197
- Cottaar, S., & Romanowicz, B. (2012). An unusually large ULVZ at the base of the mantle near Hawaii. *Earth and Planetary Science Letters*, 355, 213–222. doi: 10.1016/j.epsl.2012.09.005
- Dahmen, N., Clinton, J., Stähler, S., Meier, M.-A., Ceylan, S., Euchner, F., ... others (2024). Re-

- 768 visiting Martian seismicity with deep learning-based denoising. *Geophysical Journal Interna-*
769 *tional*, 239(1), 434–454. doi: 10.1093/gji/ggae279
- 770 Dahmen, N., Clinton, J. F., Meier, M.-A., Stähler, S. C., Ceylan, S., Kim, D., . . . Giardini,
771 D. (2022). MarsQuakeNet: A more complete marsquake catalog obtained by deep learn-
772 ing techniques. *Journal of Geophysical Research: Planets*, 127(11), e2022JE007503. doi:
773 10.1029/2022JE007503
- 774 Dalai, B., Kumar, P., Srinu, U., & Sen, M. K. (2022). De-noising receiver function data using the
775 unsupervised deep learning approach. *Geophysical Journal International*, 229(2), 737–749. doi:
776 10.1093/gji/ggab494
- 777 Darbyshire, J. (1950). Identification of microseismic activity with sea waves. *Proceedings of the*
778 *Royal Society of London. Series A. Mathematical and Physical Sciences*, 202(1070), 439–448.
779 doi: 10.1098/rspa.1950.0111
- 780 Davies, D., Kelly, E., & Filson, J. (1971). Vespa process for analysis of seismic signals. *Nature*
781 *Physical Science*, 232(27), 8–13. doi: 10.1038/physci232008a0
- 782 Dziewonski, A. M., & Anderson, D. L. (1981). Preliminary reference earth model. *Physics of the*
783 *earth and planetary interiors*, 25(4), 297–356. doi: 10.1016/0031-9201(81)90046-7
- 784 Engel, J., Gu, C., & Roberts, A. (2020). DDSP: Differentiable digital signal processing. In *Inter-*
785 *national conference on learning representations (iclr)*.
- 786 Feng, M., Chen, L., Wei, S., Muksin, U., Simanjuntak, A. V., Chen, Y., & Gong, C. (2024).
787 Deep Learning–Based Denoising Improves Receiver Function Imaging Using Dense Short-Period
788 Teleseismic Data. *Seismological Research Letters*, 95(6), 3696–3708. doi: 10.1785/0220240017
- 789 Foulger, G. R., Panza, G. F., Artemieva, I. M., Bastow, I. D., Cammarano, F., Evans, J. R.,
790 . . . others (2013). Caveats on tomographic images. *Terra Nova*, 25(4), 259–281. doi:
791 10.1111/ter.12041
- 792 Friedrich, A., Krüger, F., & Klinge, K. (1998). Ocean-generated microseismic noise located with
793 the Gräfenberg array. *Journal of seismology*, 2(1), 47–64. doi: 10.1023/A:1009788904007
- 794 Frost, D. A., Lasbleis, M., Chandler, B., & Romanowicz, B. (2021). Dynamic history of the in-
795 ner core constrained by seismic anisotropy. *Nature Geoscience*, 14(7), 531–535. doi: 10.1038/
796 s41561-021-00761-w
- 797 Gaci, S. (2013). The use of wavelet-based denoising techniques to enhance the first-arrival picking
798 on seismic traces. *IEEE Transactions on Geoscience and Remote Sensing*, 52(8), 4558–4563.
799 doi: 10.1109/TGRS.2013.2282422
- 800 Ge, W., Mao, Q., Zhou, W., Gui, Z., & Wang, P. (2024). Signal enhancement for downhole micro-
801 seismic data using improved attention mechanism based on autoencoder network. *IEEE Access*.
802 doi: 10.1109/ACCESS.2024.3483196
- 803 Han, J., & van der Baan, M. (2015). Microseismic and seismic denoising via ensemble empirical
804 mode decomposition and adaptive thresholding. *Geophysics*, 80(6), KS69–KS80. doi: 10.1190/
805 geo2014-0423.1
- 806 Hansen, S. E., Garnero, E. J., Li, M., Shim, S.-H., & Rost, S. (2023). Globally distributed sub-
807 ducted materials along the Earth’s core-mantle boundary: Implications for ultralow velocity
808 zones. *Science Advances*, 9(14), eadd4838. doi: 10.1126/sciadv.add4838
- 809 Hansen, S. E., Garnero, E. J., & Rost, S. (2021). Historical interstation pattern referencing
810 (HIPR): An application to PcP waves recorded in the Antarctic for ULVZ imaging. *Journal of*
811 *Geophysical Research: Solid Earth*, 126(10), e2021JB022741. doi: 10.1029/2021JB022741
- 812 Heuel, J., & Friederich, W. (2022). Suppression of wind turbine noise from seismological data us-
813 ing nonlinear thresholding and denoising autoencoder. *Journal of Seismology*, 26(5), 913–934.
814 doi: 10.1007/s10950-022-10097-6
- 815 Hutko, A. R., Bahavar, M., Trabant, C., Weekly, R. T., Fossen, M. V., & Ahern, T. (2017). Data
816 products at the IRIS-DMC: Growth and usage. *Seismological Research Letters*, 88(3), 892–903.
817 doi: 10.1785/0220160190
- 818 Iman, M., Arabnia, H. R., & Rasheed, K. (2023). A review of deep transfer learning and recent
819 advancements. *Technologies*, 11(2), 40. doi: 10.3390/technologies11020040
- 820 Ioffe, S., & Szegedy, C. (2015). Batch normalization: Accelerating deep network training by re-

821 ducing internal covariate shift. In *International conference on machine learning* (pp. 448–456).

822 Iyer, H. (1958). A study on the direction of arrival of microseisms at kew observatory. *Geophysical*
823 *Journal International*, 1(1), 32–43. doi: 10.1111/j.1365-246X.1958.tb00032.x

824 Jackson, J. M., & Thomas, C. (2021). Seismic and mineral physics constraints on the d'' layer.
825 *Mantle convection and surface expressions*, 193–227. doi: 10.1002/9781119528609.ch8

826 Jagt, L., Martin, C., Millet, F., Russell, S., & Cottaar, S. (2024). Pdiff Postcursors from the Base
827 of the Hawaiian ULVZ. *The Seismic Record*, 4(3), 204–213. doi: 10.1785/0320240016

828 Kanasewich, E., Alpaslan, T., & Hemmings, C. (1973). Nth-root stack nonlinear multichannel fil-
829 ter. *Geophysics*, 38(2), 327–338. doi: 10.1190/1.1440343

830 Komatitsch, D. (2011). Fluid–solid coupling on a cluster of gpu graphics cards for seismic wave
831 propagation. *Comptes Rendus Mecanique*, 339(2-3), 125–135. doi: 10.1016/j.crme.2010.11.007

832 Komatitsch, D., & Tromp, J. (1999). Introduction to the spectral element method for three-
833 dimensional seismic wave propagation. *Geophysical journal international*, 139(3), 806–822. doi:
834 10.1046/j.1365-246x.1999.00967.x

835 Komatitsch, D., & Tromp, J. (2002). Spectral-element simulations of global seismic wave propa-
836 gation—II. Three-dimensional models, oceans, rotation and self-gravitation. *Geophysical journal*
837 *international*, 150(1), 303–318. doi: 10.1046/j.1365-246X.2002.01716.x

838 Krischer, L., Hutko, A. R., van Driel, M., Stähler, S., Bahavar, M., Trabant, C., & Nissen-Meyer,
839 T. (2017, 04). On-Demand Custom Broadband Synthetic Seismograms. *Seismological Research*
840 *Letters*, 88(4), 1127–1140. doi: 10.1785/0220160210

841 Lai, V. H., Helmberger, D. V., Dobrosavljevic, V. V., Wu, W., Sun, D., Jackson, J. M., & Gurnis,
842 M. (2022). Strong ULVZ and slab interaction at the northeastern edge of the Pacific LLSVP
843 favors plume generation. *Geochemistry, Geophysics, Geosystems*, 23(2), e2021GC010020. doi:
844 10.1029/2021GC010020

845 Langston, C. A., & Mousavi, S. M. (2019). Separating signal from noise and from other signal us-
846 ing nonlinear thresholding and scale-time windowing of continuous wavelet transforms. *Bulletin*
847 *of the Seismological Society of America*, 109(5), 1691–1700. doi: 10.1785/0120190073

848 Leng, K., Nissen-Meyer, T., & van Driel, M. (2016). Efficient global wave propagation adapted
849 to 3-D structural complexity: a pseudospectral/spectral-element approach. *Geophysical Sup-*
850 *plements to the Monthly Notices of the Royal Astronomical Society*, 207(3), 1700–1721. doi:
851 10.1093/gji/ggw363

852 Leng, K., Nissen-Meyer, T., Van Driel, M., Hosseini, K., & Al-Attar, D. (2019). AxiSEM3D:
853 broad-band seismic wavefields in 3-D global earth models with undulating discontinuities. *Geo-*
854 *physical Journal International*, 217(3), 2125–2146. doi: 10.1093/gji/ggz092

855 Li, J., Qu, R., & Lu, C. (2023). Multiple attention mechanisms-based convolutional neural net-
856 work for desert seismic denoising. *Pure and Applied Geophysics*, 180(6), 2135–2155. doi: 10
857 .1007/s00024-023-03255-5

858 Li, J., Sun, D., & Bower, D. J. (2022). Slab control on the mega-sized north pacific ultra-low ve-
859 locity zone. *Nature Communications*, 13(1), 1042. doi: 10.1038/s41467-022-28708-8

860 Li, Z., Leng, K., Jenkins, J., & Cottaar, S. (2022). Kilometer-scale structure on the core–mantle
861 boundary near Hawaii. *Nature Communications*, 13(1), 2787. doi: 10.1038/s41467-022-30502
862 -5

863 Li, Z., Martin, C., & Cottaar, S. (2024). Seismic observation of a new ULVZ beneath the South-
864 ern Pacific. *Journal of Geophysical Research: Solid Earth*, 129(4), e2023JB026941. doi: 10
865 .1029/2023JB026941

866 Lin, H., Xu, J., Xing, L., Li, Q., & Liu, H. (2024). Random noise attenuation of ocean bot-
867 tom seismometers based on a substep deep denoising autoencoder. *Geophysical Prospecting*,
868 72(Special Issue: Seabed Prospecting Technology), 1428–1441. doi: 10.1111/1365-2478.13302

869 Liu, J.-Y., & Yang, Y.-H. (2018). Denoising auto-encoder with recurrent skip connections and
870 residual regression for music source separation. In *2018 17th ieee international conference on*
871 *machine learning and applications (icmla)* (pp. 773–778). doi: 10.1109/ICMLA.2018.00123

872 Longuet-Higgins, M. S. (1950). A theory of the origin of microseisms. *Philosophical Transactions*
873 *of the Royal Society of London. Series A, Mathematical and Physical Sciences*, 243(857), 1–35.

874 doi: 10.1098/rsta.1950.0012

875 Lythgoe, K., Deuss, A., Rudge, J., & Neufeld, J. (2014). Earth’s inner core: Innermost inner core
876 or hemispherical variations? *Earth and Planetary Science Letters*, *385*, 181–189. doi: 10.1016/
877 j.epsl.2013.10.049

878 Ma, Z., Li, H., Liu, M., Huang, Y., Zhang, S., & Lv, Y. (2023). Micro-seismic events detection
879 and its tectonic implications in Northeastern Hainan Province. *Frontiers in Earth Science*, *11*,
880 1169877. doi: 10.3389/feart.2023.1169877

881 Martin, C., Bodin, T., & Cottaar, S. (2023a). Mapping structures on the core–mantle boundary
882 using Sdiff postcursors: Part II. Application to the Hawaiian ULVZ. *Geophysical Journal Inter-
883 national*, *235*(3), 2399–2409. doi: 10.1093/gji/ggad345

884 Martin, C., Bodin, T., & Cottaar, S. (2023b). Mapping structures on the core–mantle bound-
885 ary using Sdiff postcursors: Part I. Method and Validation. *Geophysical Journal International*,
886 *235*(3), 2385–2398. doi: 10.1093/gji/ggad340

887 Martin, C., Harmsma, L., Atkins, J., Deuss, A., & Cottaar, S. (2025). Evidence of a ULVZ near
888 Vanuatu from Sdiff postcursors. *Journal of Studies of Earth’s Deep Interior*, *1*(1). doi: 10
889 .46298/jsedi.15883

890 Martin, C., Russell, S., & Cottaar, S. (2024). Detection of a ULVZ in the Central Pacific using
891 high frequency Sdiff postcursors. *Earth and Planetary Science Letters*, *648*, 119028. doi: 10
892 .1016/j.epsl.2024.119028

893 McNamara, A. K. (2019). A review of large low shear velocity provinces and ultra low velocity
894 zones. *Tectonophysics*, *760*, 199–220. doi: 10.1016/j.tecto.2018.04.015

895 Mousavi, S. M., & Beroza, G. C. (2022). Deep-learning seismology. *Science*, *377*(6607),
896 eabm4470. doi: 10.1126/science.abm4470

897 Mousavi, S. M., Langston, C. A., & Horton, S. P. (2016). Automatic microseismic denoising and
898 onset detection using the synchrosqueezed continuous wavelet transform. *Geophysics*, *81*(4),
899 V341–V355. doi: 10.1190/geo2015-0598.1

900 Nissen-Meyer, T., van Driel, M., Stähler, S. C., Hosseini, K., Hempel, S., Auer, L., ... Fournier,
901 A. (2014). AxiSEM: broadband 3-D seismic wavefields in axisymmetric media. *Solid Earth*,
902 *5*(1), 425–445. doi: 10.5194/se-5-425-2014

903 Oboué, Y. A. S. I., Ying, H., Ma, S., Zuo, P., & Chen, Y. (2026). Deep Learning-Based Recovery
904 of Weak PcP Phases from Noisy Seismic Records. *Big Data and Earth System*, 100041. doi: 10
905 .1016/j.bdes.2026.100041

906 Okada, Y., Kasahara, K., Hori, S., Obara, K., Sekiguchi, S., Fujiwara, H., & Yamamoto, A.
907 (2004). Recent progress of seismic observation networks in japan—hi-net, f-net, k-net and
908 kik-net—. *Earth, Planets and Space*, *56*(8), xv–xxviii. doi: 10.1186/BF03353076

909 Oldham, R. D. (1906). The constitution of the interior of the Earth, as revealed by earthquakes.
910 *Quarterly Journal of the Geological Society*, *62*(1-4), 456–475.

911 Othman, A., Iqbal, N., Hanafy, S. M., & Waheed, U. B. (2021). Automated event detec-
912 tion and denoising method for passive seismic data using residual deep convolutional neu-
913 ral networks. *IEEE Transactions on Geoscience and Remote Sensing*, *60*, 1–11. doi:
914 10.1109/TGRS.2021.3054071

915 Ringler, A. T., Anthony, R. E., Aster, R., Ammon, C., Arrowsmith, S., Benz, H., ... others
916 (2022). Achievements and prospects of global broadband seismographic networks after 30 years
917 of continuous geophysical observations. *Reviews of Geophysics*, *60*(3), e2021RG000749. doi:
918 10.1029/2021RG000749

919 Ringler, A. T., Steim, J., Wilson, D. C., Widmer-Schmidrig, R., & Anthony, R. E. (2020). Im-
920 provements in seismic resolution and current limitations in the Global Seismographic Network.
921 *Geophysical Journal International*, *220*(1), 508–521. doi: 10.1093/gji/ggz473

922 Romanowicz, B. A., & Dziewonski, A. M. (1987). Global digital seismographic network: Research
923 opportunities and recent initiatives. *Composition, structure and dynamics of the lithosphere-
924 asthenosphere system*, *16*, 99–110. doi: 10.1029/GD016p0099

925 Ronneberger, O., Fischer, P., & Brox, T. (2015). U-net: Convolutional networks for biomedical
926 image segmentation. In *Medical image computing and computer-assisted intervention–miccai*

- 927 2015: 18th international conference, munich, germany, october 5-9, 2015, proceedings, part iii
928 18 (pp. 234–241). doi: 10.1007/978-3-319-24574-4_28
- 929 Rost, S., & Thomas, C. (2002). Array seismology: Methods and applications. *Reviews of geo-*
930 *physics*, 40(3), 2–1. doi: 10.1029/2000RG000100
- 931 Rost, S., & Thomas, C. (2009). Improving seismic resolution through array processing techniques.
932 *Surveys in geophysics*, 30, 271–299. doi: 10.1007/s10712-009-9070-6
- 933 Ruan, Y., Lei, W., Modrak, R., Örsvuran, R., Bozdağ, E., & Tromp, J. (2019). Balancing un-
934 evenly distributed data in seismic tomography: a global adjoint tomography example. *Geophys-*
935 *ical Journal International*, 219(2), 1225–1236. doi: 10.1093/gji/ggz356
- 936 Russell, S., Magali, J. K., Vallenton, K., & Thomas, C. (2025). The effect of source-side subduc-
937 tion on PKP differential times and implications for inner core anisotropy. *Physics of the Earth*
938 *and Planetary Interiors*, 107382. doi: 10.1016/j.pepi.2025.107382
- 939 Schimmel, M., & Paulssen, H. (1997). Noise reduction and detection of weak, coherent signals
940 through phase-weighted stacks. *Geophysical Journal International*, 130(2), 497–505. doi: 10
941 .1111/j.1365-246X.1997.tb05664.x
- 942 Schweitzer, J., Fyen, J., Mykkeltveit, S., Gibbons, S. J., PIRLI, M., Kühn, D., & Kväerna, T.
943 (2012). Seismic arrays. In *New manual of seismological observatory practice 2 (nmsop-2)*
944 (pp. 1–80). Deutsches GeoForschungsZentrum GFZ.
- 945 Shi, Q., & Denolle, M. A. (2023). Improved observations of deep earthquake ruptures using ma-
946 chine learning. *Journal of Geophysical Research: Solid Earth*, 128(12), e2023JB027334. doi: 10
947 .1029/2023JB027334
- 948 Shi, Q., Denolle, M. A., Ni, Y., Williams, E. F., & You, N. (2025). Denoising offshore distributed
949 acoustic sensing using masked auto-encoders to enhance earthquake detection. *Journal of Geo-*
950 *physical Research: Solid Earth*, 130(2), e2024JB029728. doi: 10.1029/2024JB029728
- 951 Srivastava, N., Hinton, G., Krizhevsky, A., Sutskever, I., & Salakhutdinov, R. (2014). Dropout:
952 a simple way to prevent neural networks from overfitting. *The journal of machine learning re-*
953 *search*, 15(1), 1929–1958.
- 954 Steinberg, A., Gaebler, P., Hartmann, G., Lehr, J., & Pilger, C. (2024). Deep Neural Networks
955 Based Denoising of Regional Seismic Waveforms and Impact on Analysis of North Korean
956 Nuclear Tests. *Pure and Applied Geophysics*, 1–21. doi: 10.1007/s00024-024-03491-3
- 957 Stephenson, J., Tkalčić, H., & Sambridge, M. (2021). Evidence for the innermost inner core: ro-
958 bust parameter search for radially varying anisotropy using the neighborhood algorithm. *Jour-*
959 *nal of Geophysical Research: Solid Earth*, 126(1), e2020JB020545. doi: 10.1029/2020JB020545
- 960 Thorne, M. S., Garnero, E. J., Jahnke, G., Igel, H., & McNamara, A. K. (2013). Mega ultra low
961 velocity zone and mantle flow. *Earth and Planetary Science Letters*, 364, 59–67. doi: 10.1016/
962 j.epsl.2012.12.034
- 963 Thorne, M. S., Leng, K., Pachhai, S., Rost, S., Wicks, J., & Nissen-Meyer, T. (2021). The most
964 parsimonious ultralow-velocity zone distribution from highly anomalous SPdKS waveforms.
965 *Geochemistry, Geophysics, Geosystems*, 22(1), e2020GC009467. doi: 10.1029/2020GC009467
- 966 Tian, D. (2024). HinetPy: A Python package for accessing and processing NIED Hi-net seismic
967 data. *Journal of Open Source Software*, 9(98), 6840. doi: 10.21105/joss.06840
- 968 Tibi, R., Hammond, P., Brogan, R., Young, C. J., & Koper, K. (2021). Deep learning denois-
969 ing applied to regional distance seismic data in Utah. *Bulletin of the Seismological Society of*
970 *America*, 111(2), 775–790. doi: 10.1785/0120200292
- 971 Tibi, R., Young, C. J., & Porritt, R. W. (2023). Comparative study of the performance of seis-
972 mic waveform denoising methods using local and near-regional data. *Bulletin of the Seismologi-*
973 *cal Society of America*, 113(2), 548–561. doi: 10.1785/0120220105
- 974 van Driel, M., Kemper, J., & Boehm, C. (2021). On the modelling of self-gravitation for full 3-d
975 global seismic wave propagation. *Geophysical Journal International*, 227(1), 632–643. doi: 10
976 .1093/gji/ggab237
- 977 van Driel, M., Krischer, L., Stähler, S. C., Hosseini, K., & Nissen-Meyer, T. (2015). Instaseis:
978 instant global seismograms based on a broadband waveform database. *Solid Earth*, 6(2), 701–
979 717. doi: 10.5194/se-6-701-2015,2015.

- 980 Viens, L., & Van Houtte, C. (2020). Denoising ambient seismic field correlation functions with
981 convolutional autoencoders. *Geophysical Journal International*, *220*(3), 1521–1535. doi: 10
982 .1093/gji/ggz509
- 983 Waszek, L., Irving, J., Phạm, T.-S., & Tkalčić, H. (2023). Seismic insights into Earth’s core. *na-
984 ture communications*, *14*(1), 6029. doi: 10.1038/s41467-023-41725-5
- 985 Weiss, K., Khoshgoftaar, T. M., & Wang, D. (2016). A survey of transfer learning. *Journal of Big
986 data*, *3*(1), 9. doi: 10.1186/s40537-016-0043-6
- 987 Wilson, D. C., Hutt, C. R., Gee, L. S., Ringler, A. T., & Anthony, R. E. (2024). Global seismic
988 networks operated by the US Geological Survey. *Seismological Research Letters*, *95*(3), 1578–
989 1590. doi: 10.1785/0220230178
- 990 Wolf, J., & Long, M. D. (2023). Lowermost mantle structure beneath the central Pacific Ocean:
991 Ultralow velocity zones and seismic anisotropy. *Geochemistry, Geophysics, Geosystems*, *24*(6),
992 e2022GC010853. doi: 10.1029/2022GC010853
- 993 Wolf, J., Long, M. D., & Frost, D. A. (2024). Ultralow velocity zone and deep mantle flow be-
994 neath the Himalayas linked to subducted slab. *Nature Geoscience*, *17*(4), 302–308. doi: 10
995 .1038/s41561-024-01386-5
- 996 Yamamoto, R., Song, E., & Kim, J.-M. (2020). Parallel wavegan: A fast waveform generation
997 model based on generative adversarial networks with multi-resolution spectrogram. In *Icassp
998 2020-2020 ieee international conference on acoustics, speech and signal processing (icassp)* (pp.
999 6199–6203).
- 1000 Yang, L., Liu, X., Zhu, W., Zhao, L., & Beroza, G. C. (2022). Toward improved urban earthquake
1001 monitoring through deep-learning-based noise suppression. *Science advances*, *8*(15), eabl3564.
1002 doi: 10.1126/sciadv.abl3564
- 1003 Yu, S., & Garnero, E. J. (2018). Ultralow velocity zone locations: A global assessment. *Geochem-
1004 istry, Geophysics, Geosystems*, *19*(2), 396–414. doi: 10.1002/2017GC007281
- 1005 Yuan, K., & Romanowicz, B. (2017). Seismic evidence for partial melting at the root of major hot
1006 spot plumes. *Science*, *357*(6349), 393–397. doi: 10.1126/science.aan076
- 1007 Zhou, J., Phạm, T.-S., & Tkalčić, H. (2024). Deep-learning phase-onset picker for deep
1008 Earth seismology: PKIKP waves. *Journal of Geophysical Research: Solid Earth*, *129*(9),
1009 e2024JB029360. doi: 10.1029/2024JB029360
- 1010 Zhu, W., Mousavi, S. M., & Beroza, G. C. (2019). Seismic signal denoising and decomposition
1011 using deep neural networks. *IEEE Transactions on Geoscience and Remote Sensing*, *57*(11),
1012 9476–9488. doi: 10.1109/TGRS.2019.2926772

Supplementary Materials for:
Denoising teleseismic data for deep Earth studies using a supervised deep-learning auto-encoder: a case study of diffracted waves from ULVZs

Stuart Russell^{*,1,2}, Katrin Hannemann¹, Carl Martin^{3,4}, Bennet Lindhorst¹,
Waleed Esmail⁵, Christine Thomas^{1,6}

¹ Institut für Geophysik, Universität Münster, Correnstraße 24, 48149, Münster, Germany

² James Cook University, 1 James Cook Drive, Douglas, QLD, 4814, Australia

³ Department of Geosciences, Utrecht University, 3584 CB, Netherlands

⁴ Research School of Earth Science, The Australian National University, Canberra, ACT, Australia

⁵ Institut für Kernphysik, Universität Münster, Wilhelm-Klemm-Straße 9, 48149, Münster

⁶ Geological Survey of Denmark and Greenland, 1350 Copenhagen, Denmark

* Corresponding author, email: stuart.russell@jcu.edu.au

Section S1: Event details

Event name	Event time (UTC)	Latitude (°N)	Longitude (°E)	Depth (km)	ULVZ sampled	Predominant station location
20090917	2009-09-17T23:21	-29.14	-112.27	10	Hawaii	Japan
20100320	2010-03-20T11:55	-3.38	152.28	418	Hawaii	Contiguous USA
20100417	2010-04-17T23:15	-6.70	147.30	418	Hawaii	Contiguous USA
20100804	2010-08-04T07:08	-5.52	146.86	220	Hawaii	Contiguous USA
20120510	2012-05-10T02:13	-28.60	-112.45	10	Hawaii	Japan
20121207	2012-12-07T18:19	-38.36	176.07	171	Pitcairn	Contiguous USA
20130511	2013-05-11T20:47	-17.94	-175.12	210	Hawaii	Contiguous USA
20131123	2013-11-23T07:48	-17.16	-176.52	370	Central Pacific	Contiguous USA
20141009	2014-10-09T02:14	-32.30	-110.92	4	Hawaii	Japan
20150519	2015-05-19T15:25	-15.36	-132.27	18	Vanuatu	Japan
20160831	2016-08-31T03:08	-3.69	152.79	499	Hawaii	Contiguous USA
20160912	2016-09-12T06:51	-28.76	-112.01	10	Galápagos	Alaska
20161225	2016-12-25T14:22	-43.41	-73.94	38	Galápagos	Alaska
20240223	2024-02-23T10:51	-35.09	-110.77	10	Hawaii	Japan

Table S1: The event details of all earthquakes referenced in this study. Events are referred to by YYYYMMDD format.

Section S2: GSN station locations

Figure S1 shows a map of the Global Seismograph Network stations that were used when training the DAE models. In total there are 199 stations for which data is available via IRIS, distributed over four network codes as shown in Table S2. The station distribution has good global coverage at all latitudes, including in the oceans as well as on the coasts and interiors of all of the continents. The GSN is expected to give a representative sample of globally distributed noise affecting teleseismic observations.

Network code	DOI	Total stations	Stations active as of Jan. 2026
CU	10.7914/SN/CU	9	9
IC	10.7914/SN/IC	10	10
II	10.7914/SN/II	59	45
IU	10.7914/SN/IU	121	76
Total:		199	140

Table S2: The details of the networks used for the GSN training dataset.

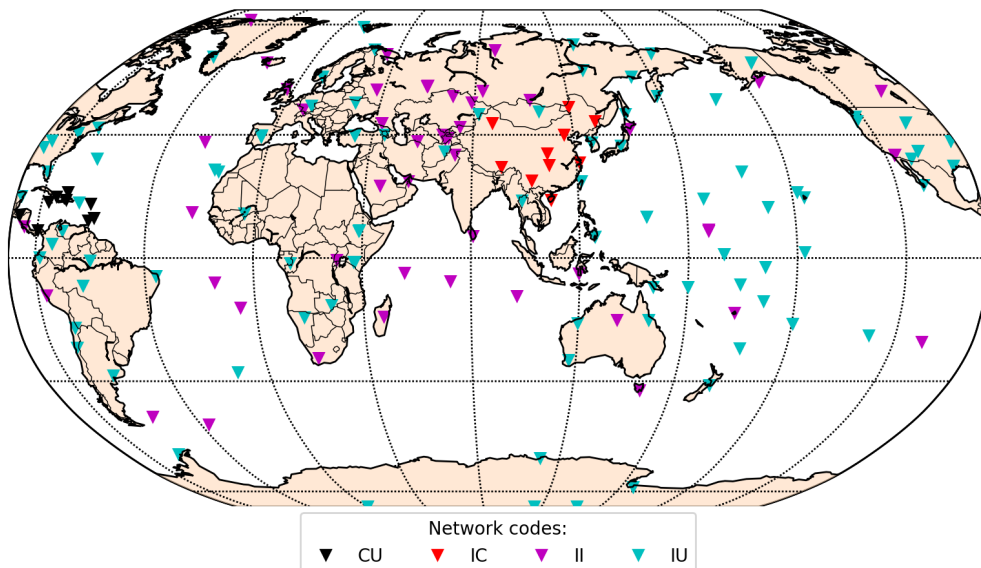


Figure S1: A map showing the locations of the GSN stations used for the GSN training dataset.

Section S3: Generation of AxiSEM3D synthetics

AxiSEM3D (Leng *et al.*, 2016, 2019) is a spectral element method (SEM) code for calculating synthetic seismograms in 3D Earth models. AxiSEM3D differs from other SEM codes by solving in a 2D computational domain and parameterising the azimuthal complexity of the wavefield as a Fourier expansion

$$u(r, \theta, \phi; t) \simeq \sum_{\alpha=0}^{N_r} u^\alpha(r, \theta; t) e^{i\alpha\phi}, \quad (1)$$

where r and θ are the in-plane directions, ϕ is the azimuthal direction, and t is the time dimension. u is the displacement field and u^α is the α th order complex Fourier coefficient field, and i is $\sqrt{-1}$. The total number of terms to be summed is N_r , which is a user-chosen parameter that can vary throughout the mesh and depends on both the complexity of the model and the desired accuracy of the simulation. For global simulations AxiSEM3D can be incredibly efficient compared to traditional SEM codes with a fully-3D computational domain, provided that a simulation is properly optimised by minimising N_r .

We minimise N_r while maximising the accuracy of S_{diff} and $S_{\text{diff}+}$ by following a similar procedure to Russell *et al.* (2025). We set N_r below a certain depth (3745 km, i.e. below the CMB), before a certain distance (60°), and beyond a certain distance (130°) to a value of 5, which is the minimum value required represent a moment tensor. The accuracy of the expansion in these regions does not affect the S_{diff} phases that we are interested in. The value elsewhere is set to 500, and we verify that this setup produces accurate waveforms. Even once optimised these simulations are still extremely costly, and computation time scales with frequency to the power 3. We run a single simulation at 4 s minimum period, which on 432 CPUs on the PALMA-II cluster of the University of Münster took 15 hours. The parameters of the simulation are summarised in Table S3 and a map of the simulation geometry, as well as synthetic waveforms are shown in Figure S2.

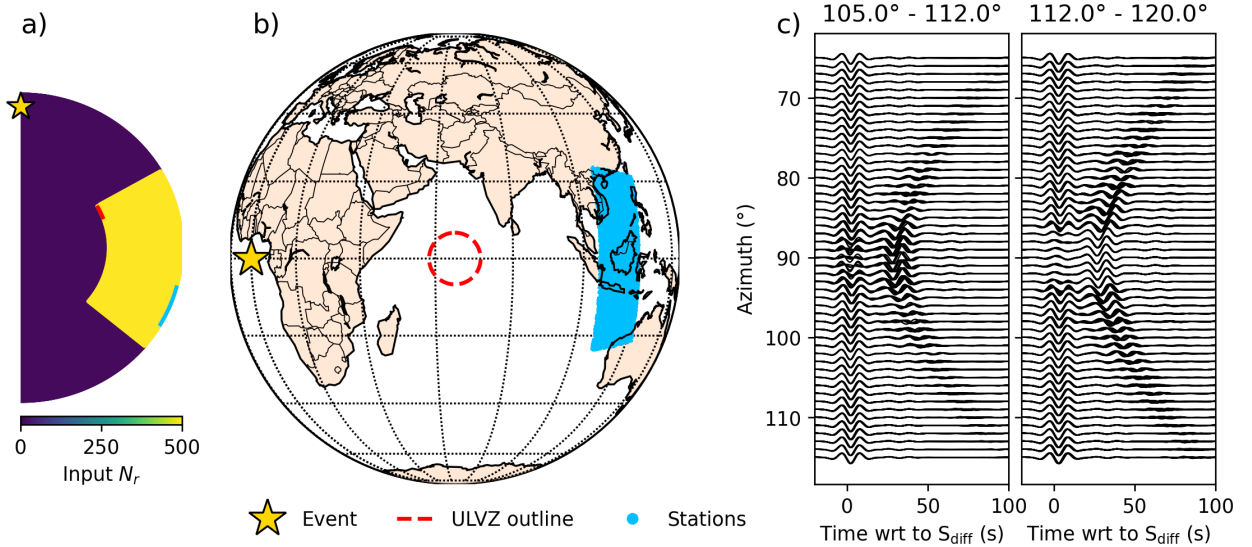


Figure S2: a) The N_r field used for the simulation shown on the 2D mesh. The locations of the event, ULVZ and stations are marked. b) Overview map of the simulation showing the position of the event, ULVZ and stations. The continents are shown to give a sense of scale, but have no meaning in the simulation. c) Example waveforms showing S_{diff} and $S_{\text{diff}+}$ for two different distance ranges indicated in the title of each plot. Traces are individually normalised such that the maximum amplitude corresponds to 0.75° azimuth, and traces are plotted rounded to the nearest degree of azimuth.

Parameter description	Value	Further remarks
General parameters		
Background model	PREM	
Minimum period	4 s	
Courant number	0.6	
Elements per wavelength	2	
Length of simulation	1,800 s	
Source parameters		
Source location	0°N, 0 °E	
Source depth	500 km	
Moment tensor	[0, 0, 0, 10 ¹³ , 0, 10 ¹³]	CMTSOLUTION format, units Nm
ULVZ parameters		
Centre of the ULVZ	0°N, 65 °E	ULVZ is cylindrical in shape
Radius of ULVZ	400 km	Approximately 6.5° at the CMB
Height of ULVZ	30 km	
S-velocity reduction inside the ULVZ	-20 %	Velocity in the ULVZ is uniform
Station parameters		
Parameter recorded	Displacement	
Distance range for stations	[105°, 120°]	
Azimuth range for stations	[60°, 120°]	
Total number of stations	10,000	Stations are distributed randomly
N_r parameters		
Radius below which N_r is set to 5	3475 km	
Distance before which N_r is set to 5	60°	
Distance beyond which N_r is set to 5	130°	
N_r in all other regions	500	

Table S3: The parameters used for the AxiSEM3D simulation used to calculate the training synthetics.

Section S4: Synthetic testing - 1D synthetics

In this section we expand on the synthetic testing shown in the main paper. We download 10,000 noise traces from the US Transportable Array (FDSN network code TA) and 10,000 S_{diff} traces via Instaseis filtered from 2 - 100 s. Here we show the results for a model trained using the GSN, with Instaseis synthetics filtered 2 - 100 s. Both the noise and synthetics in the test dataset are unseen by this DAE during training.

Figures S3, S4 and S5 are an expansion of Figure 4a and 4b in the main paper. Figure S3 shows the inputs and outputs of the denoiser for 30 randomly chosen combinations of signal and noise, where the peak amplitude ratio of signal to noise is fixed at 2 (signal has twice the amplitude of the noise). Figures S4 and S5 show cases where the peak amplitude ratio is fixed at 1 (signal and noise are the same amplitude) and 0.5 (signal has half the amplitude of the noise), respectively. In all three of these cases, the signal output is fairly good as most signals are identified and extracted, although there are always some differences. The results are visibly poorer where the peak amplitude ratio is smaller, and in some cases the DAE can fail to extract signal where it is completely obscured by noise. However, these results are extremely promising: whereas the data shown in Figure S5 would be considered unusable after manual inspection, denoising reveals the presence of this signal, showing clear potential for elucidating hidden signals.

Figure S6 shows a test case where the DAE is given pure signal, and in this case it identifies the signal well. In Figure S7 we give the DAE pure noise, and the DAE identifies this almost perfectly and does not create any erroneous signal of significant amplitude. In none of our tests do we observe a DAE ‘inventing’ realistic looking signals. In Figure S7 we include a further panel, demonstrating the danger of re-normalising recovered signal after denoising. Low amplitude and spurious energy included in the signal output can be massively amplified by the normalisation, where in reality this signal is very low amplitude relative to the target phase. Despite being a common pre-plotting step to visualising record sections, re-normalising voids using the absolute amplitude as a control, and therefore should be done with caution so as not to interpret false signals.

Where signal is extracted, the phase and timing of the signal does not usually visibly change, in contrast to amplitudes which can vary significantly. Nonetheless time shifts and waveform distortion are possible, particularly where the noise level is high, and so we quantify timing and amplitude fidelity across the test dataset of 10,000 traces. The offset of the recovered arrival relative to the input is measured by cross-correlating the denoised signal trace with the clean input signal trace, and the amplitude difference is calculated using the mean-squared error between the denoised signal trace with the clean input signal trace. Differences are quantified across several imposed noise levels and results are shown in Figures S8 for amplitudes, and Figures S9 for timings; these show the distributions for five different amplitude ratios from Figure 4c and 4d in the main paper.

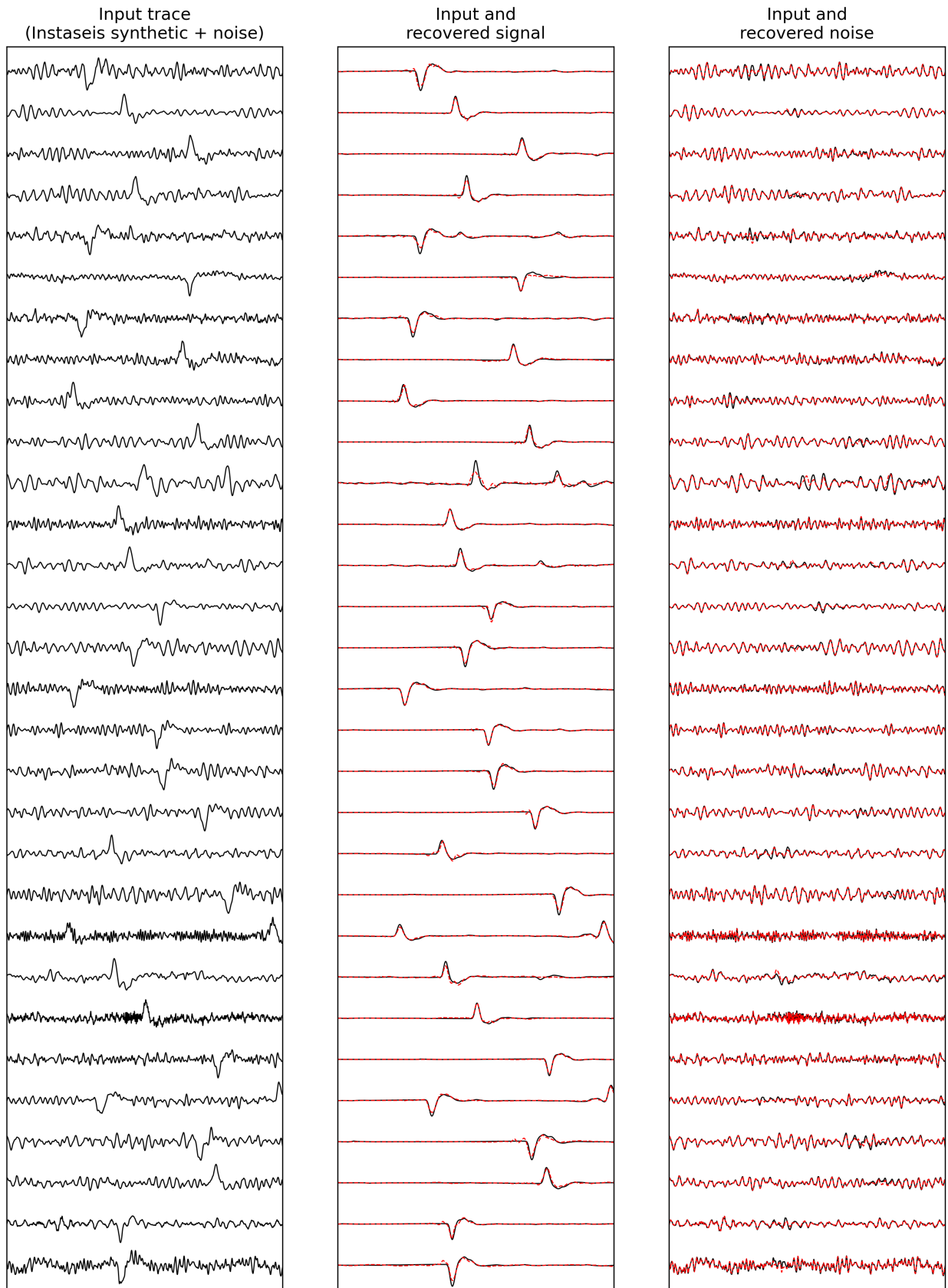


Figure S3: Application of the DAE to an unseen Instaseis synthetic test dataset where the peak amplitude ratio of signal to noise is fixed at 2. Input traces are plotted in solid black, and recovered traces are plotted on top in dashed red, with consistent amplitudes. 30 randomly selected traces are shown.

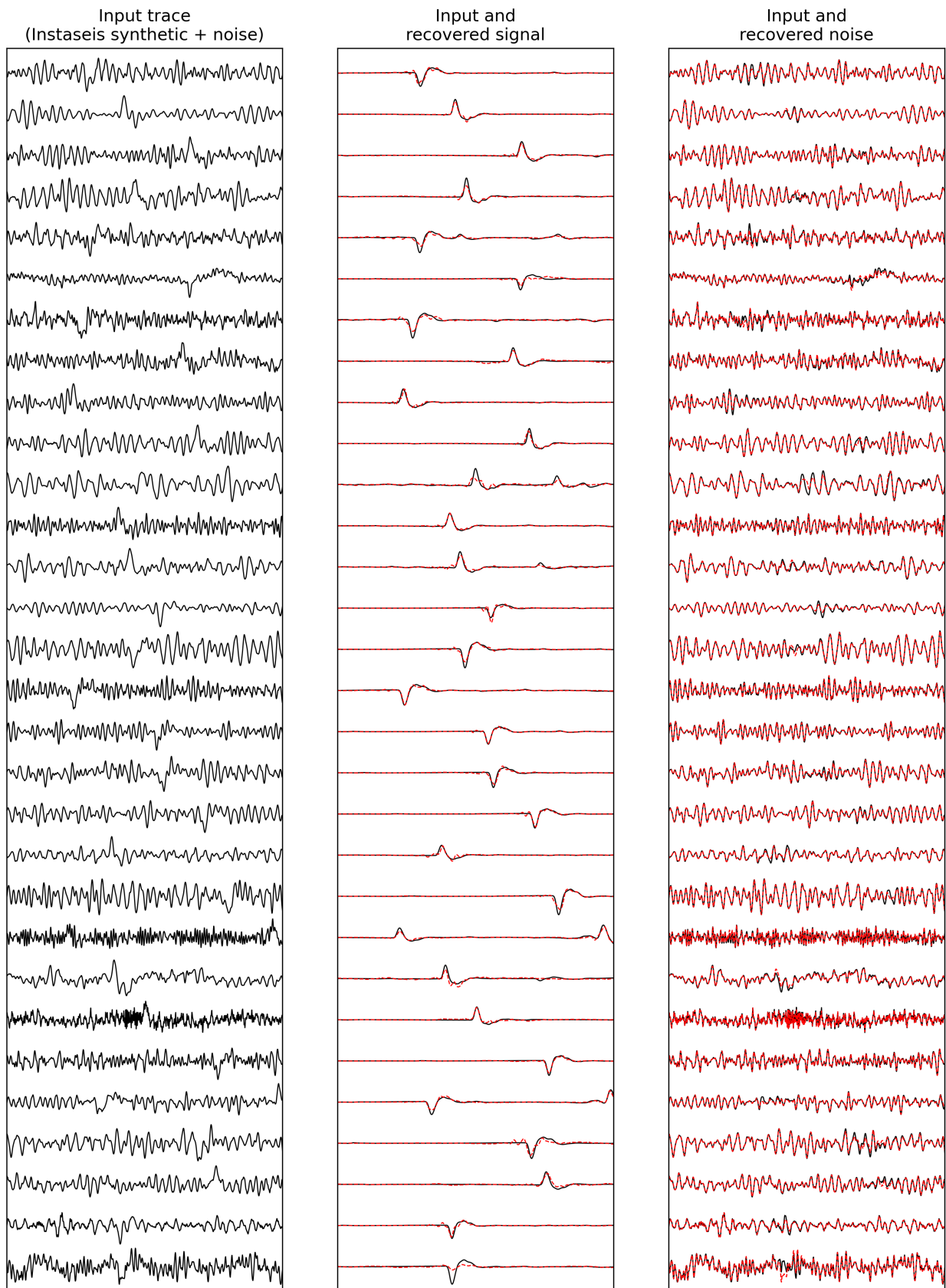


Figure S4: As for Figure S3, but where the peak amplitude ratio of signal to noise is fixed at 1.

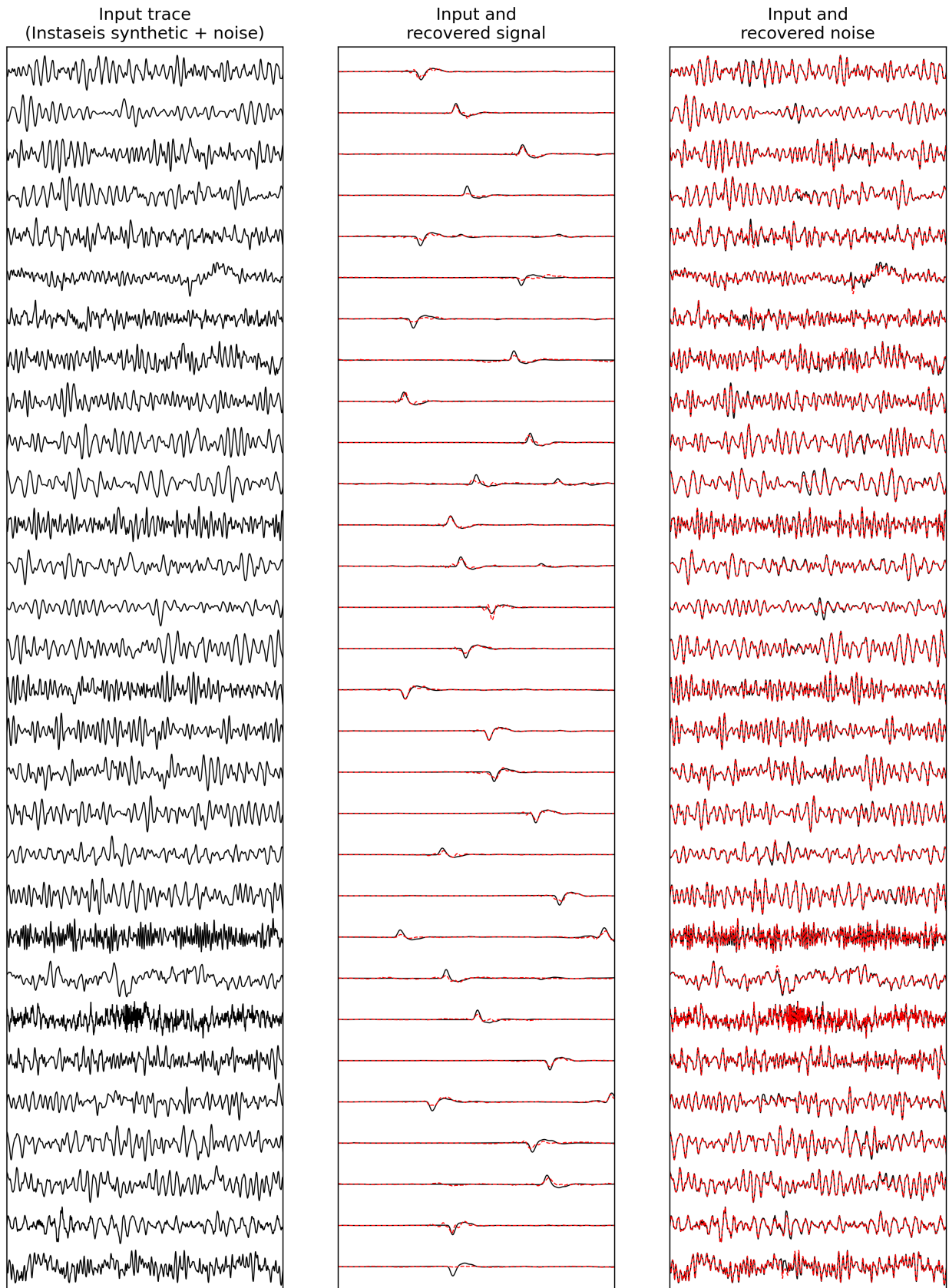


Figure S5: As for Figure S3, but where the peak amplitude ratio of signal to noise is fixed at 0.5.

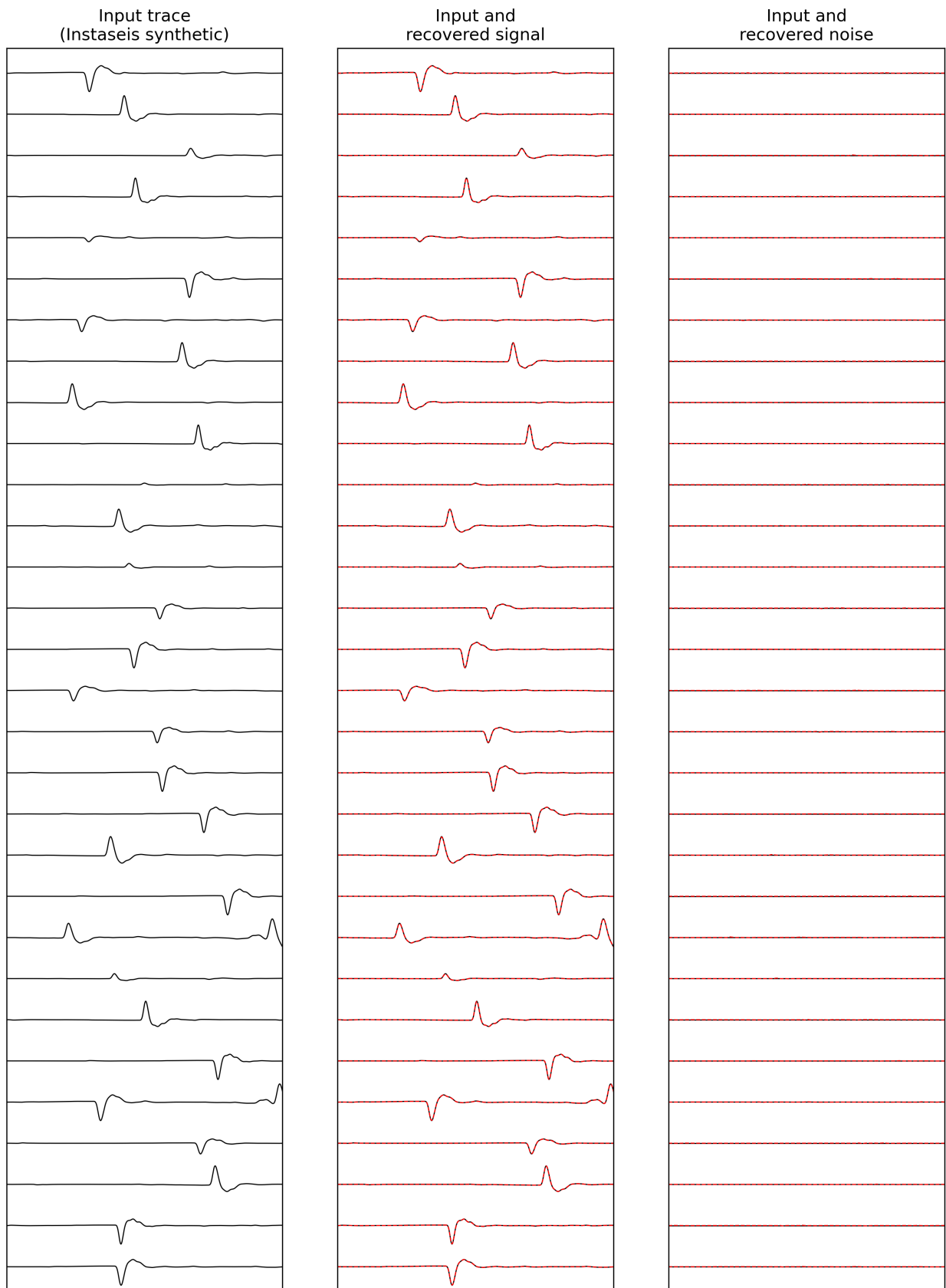


Figure S6: As for Figure S3, but where the DAE is given pure signal.

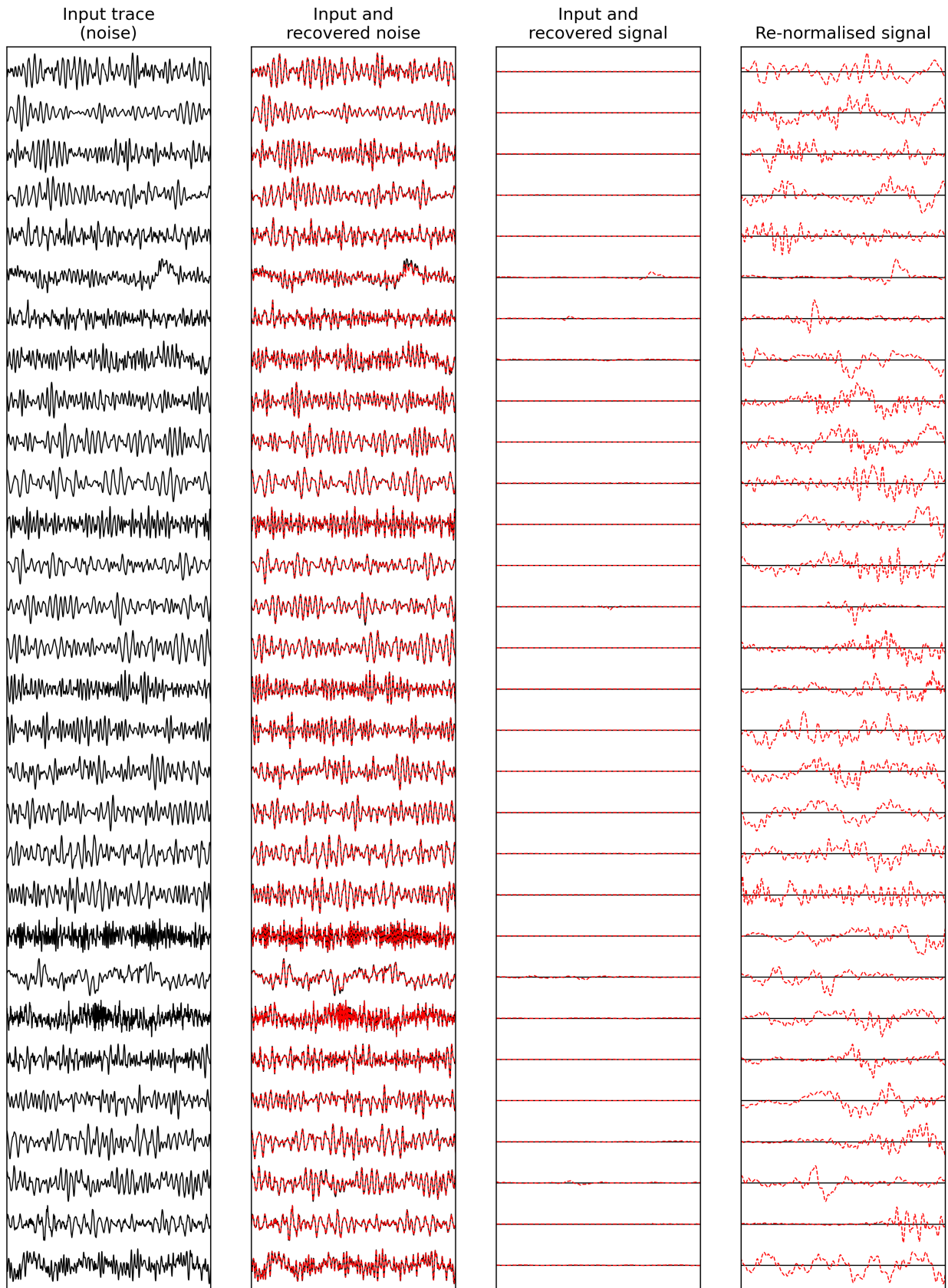


Figure S7: As for Figure S3, but where the DAE is given pure noise. An additional panel is shown where the recovered signal is re-normalised, showing the dangerous amplification of erroneous signal.

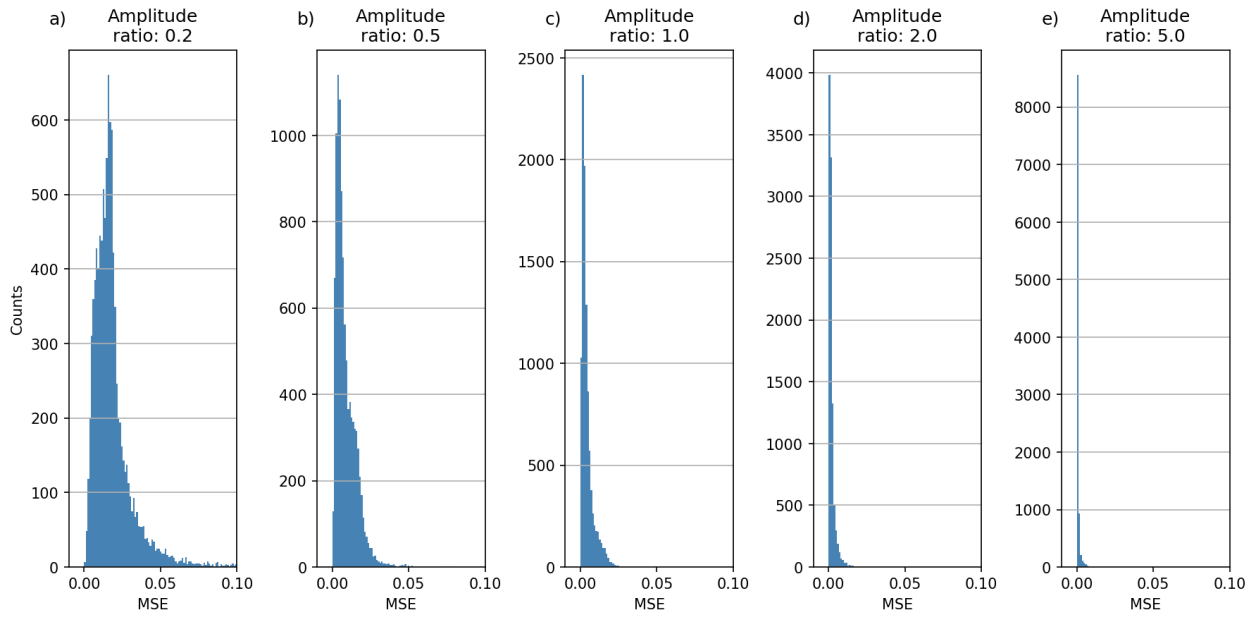


Figure S8: The mean-squared-error (MSE) of the recovered signal trace for denoising 1D synthetics for five different imposed amplitude ratios. The distribution is wider for noisier data (lower amplitude ratios).

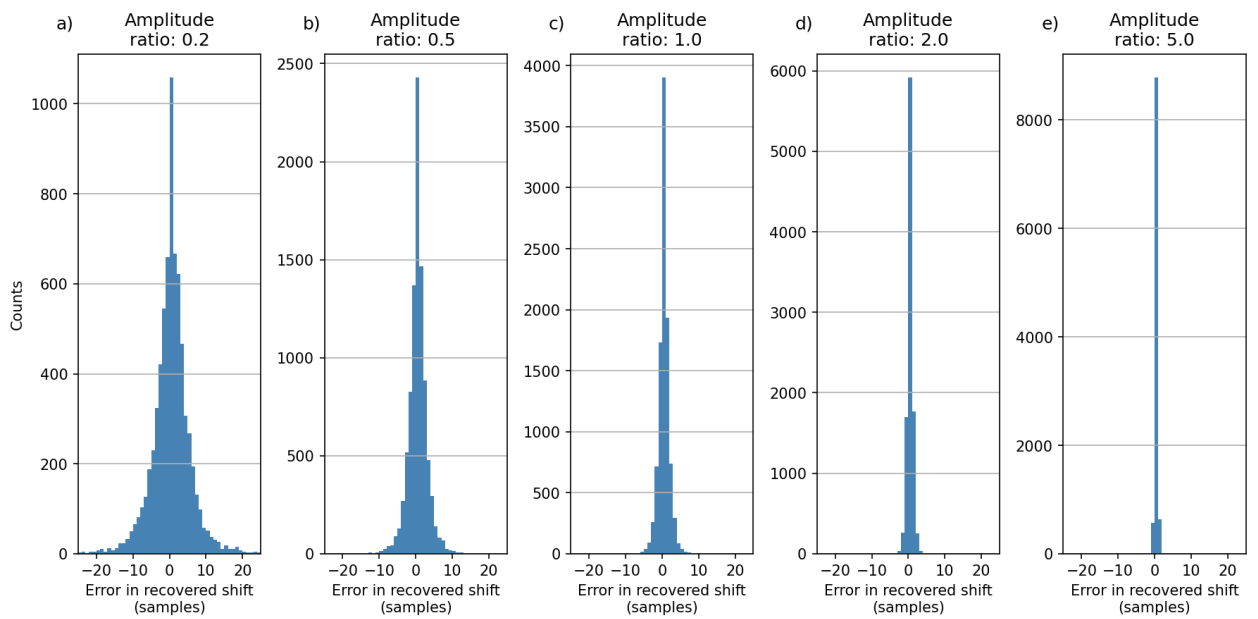


Figure S9: The error in the recovered arrival time in samples for denoising 1D synthetics for five different imposed amplitude ratios. The distribution is wider for noisier data (lower amplitude ratios).

Section S5: Synthetic testing - 3D synthetics

Beyond what is presented in the main paper, and building on what is presented in the previous section, Figures S10, S11 and S12 show the denoising of AxiSEM3D synthetics with different amplitude ratios. The results mirror the conclusions of the previous section, where extraction is better at lower noise levels, but even at high noise levels the DAE can elucidate low-amplitude signal that is obscured by the noise. In such cases, the presence of erroneous signals complicates interpretation, but these are typically low amplitude and incoherent as a function of azimuth. The DAE therefore shows great promise at screening for hidden $S_{\text{diff}+}$ – this is particularly exemplified in Figure S12 where the signals are barely visible in the input traces.

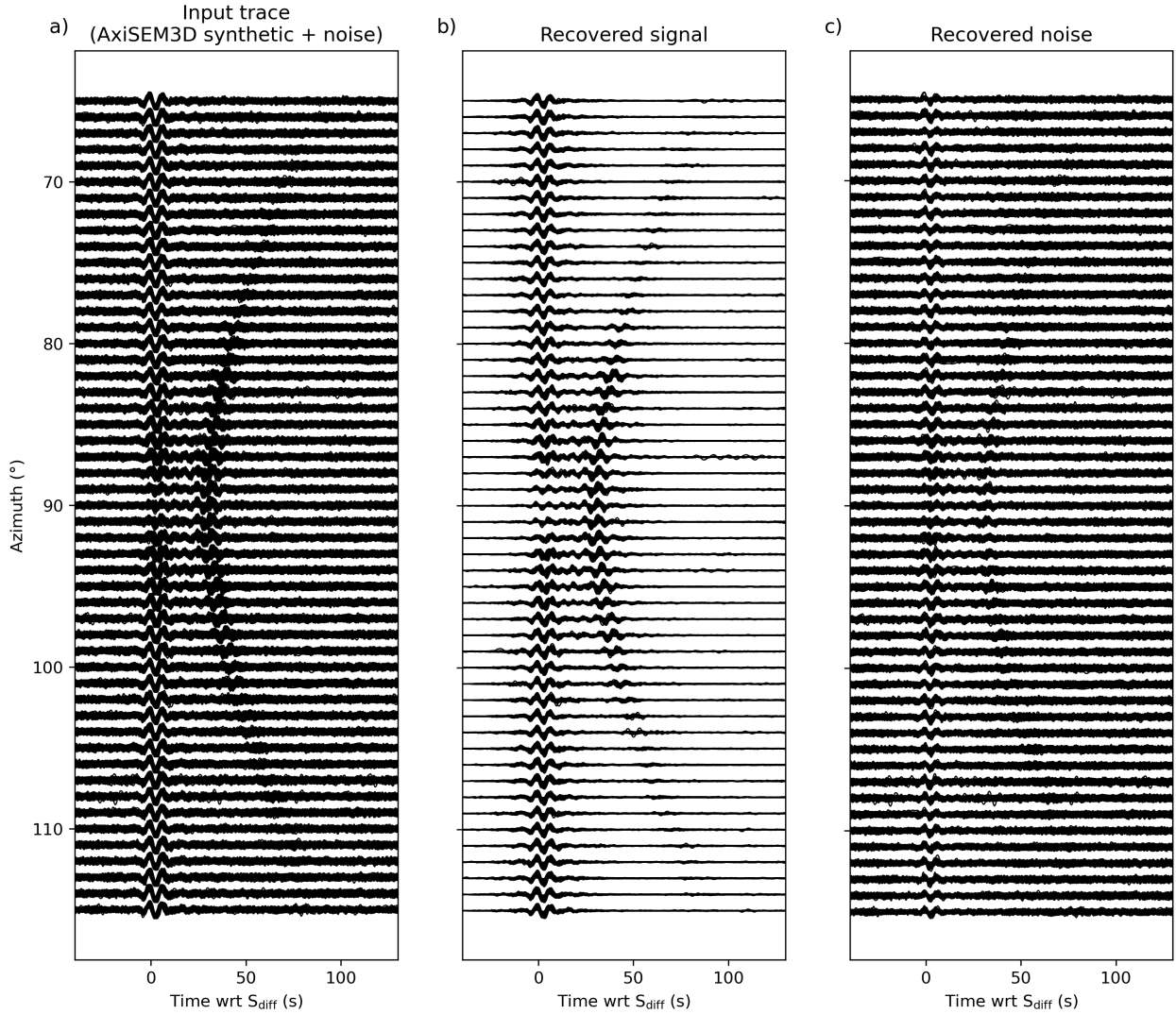


Figure S10: Application of the DAE to an unseen AxiSEM3D synthetics where the peak amplitude ratio of signal to noise is fixed at 2.0.

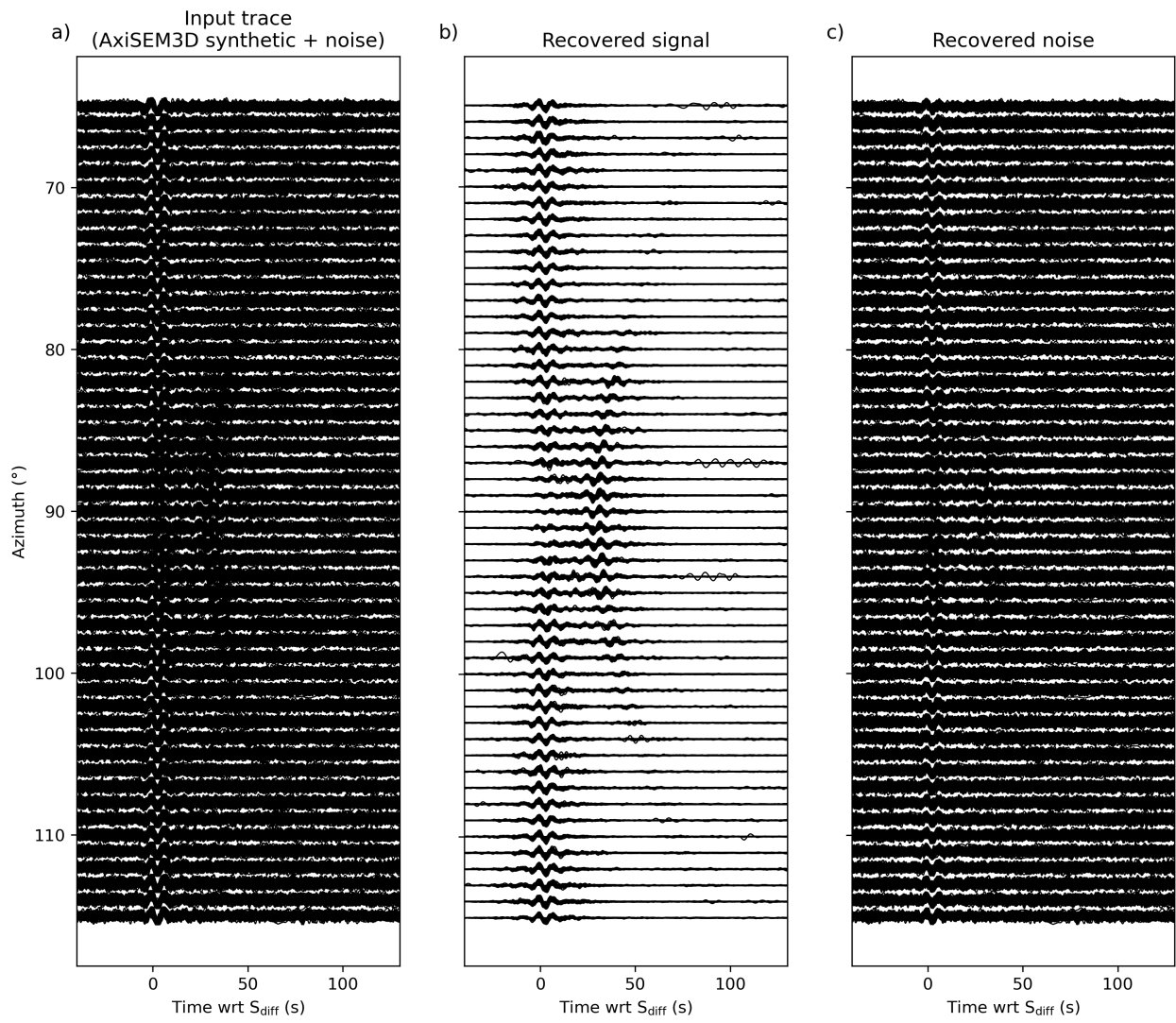


Figure S11: As for Figure S10, but where the peak amplitude ratio is fixed at 1.0.

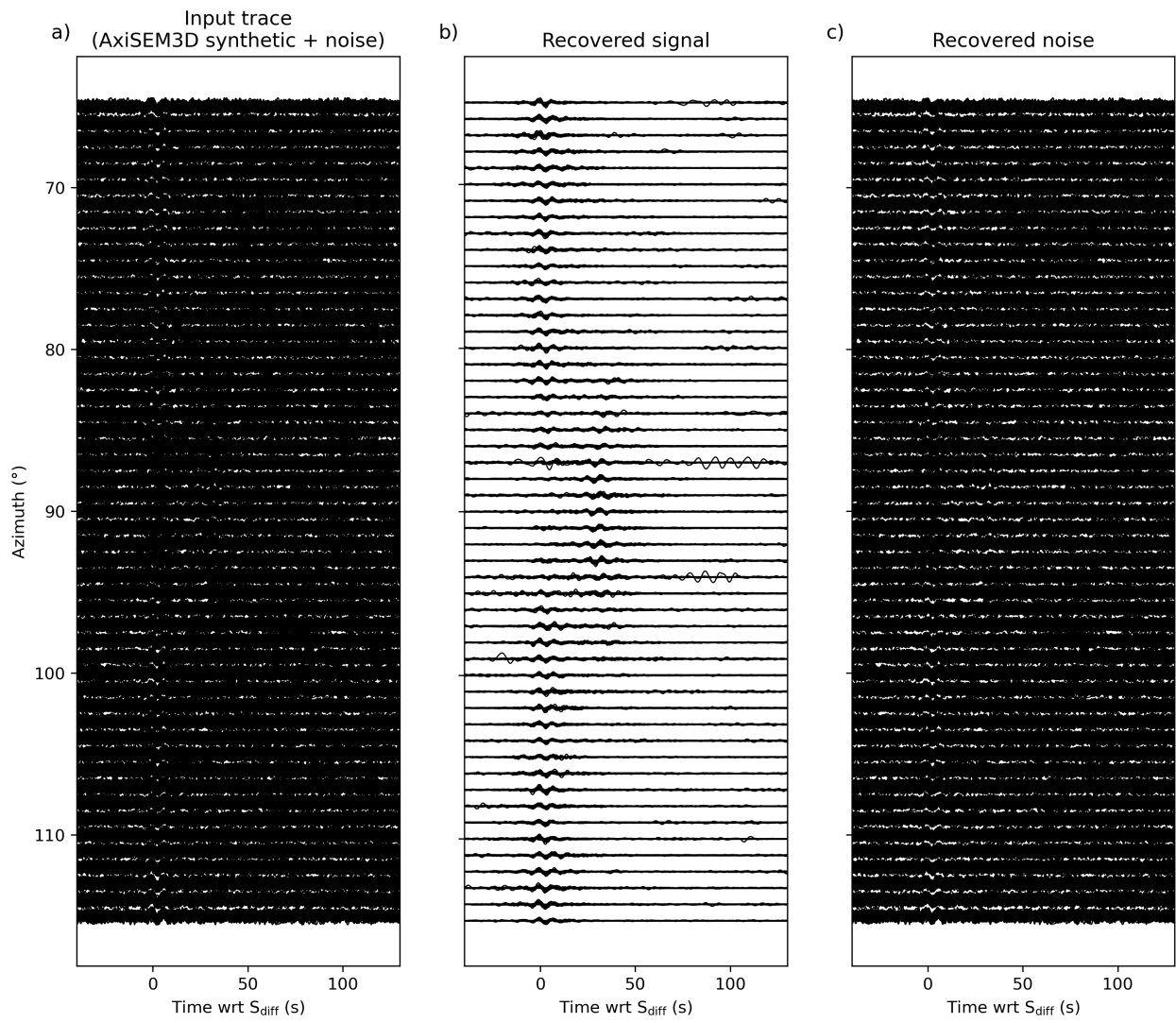


Figure S12: As for Figure S10, but where the peak amplitude ratio is fixed at 0.5.

Section S6: Noise specificity waveforms

Figures S13, S14 and S15 show the waveforms that correspond to the bars in the three panels of Figure 7 in the main paper. These data are filtered from 2.0 - 100.0 s, which is the same as the DAEs that are used for denoising.

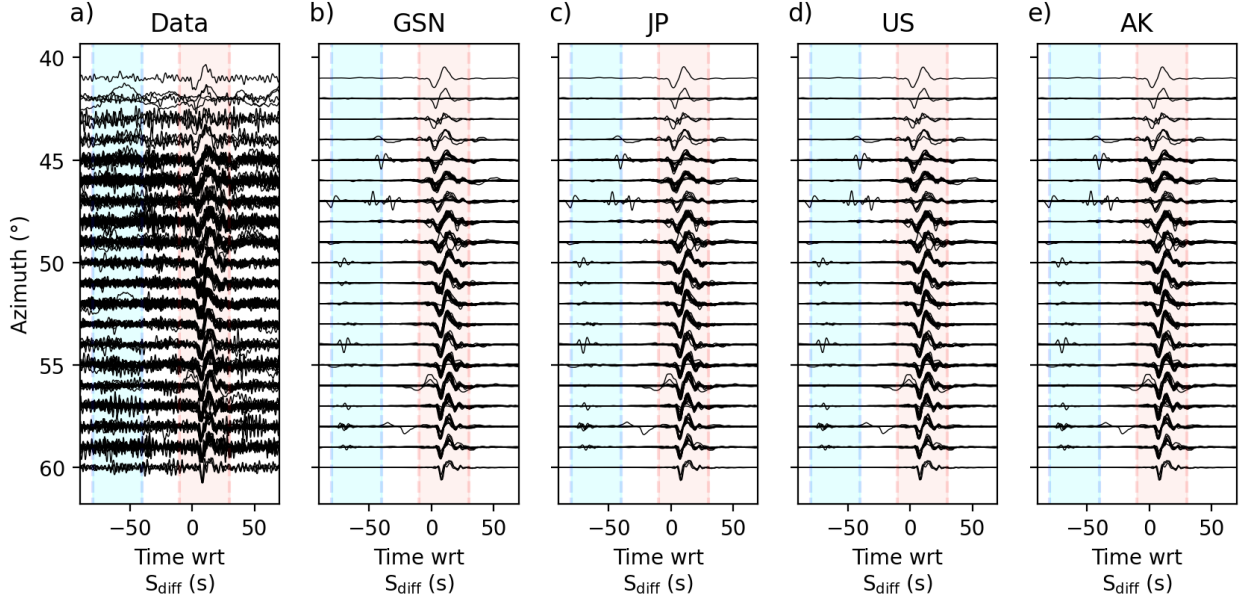


Figure S13: The waveforms corresponding to the SNR improvements shown in Figure 7 in the main paper, for event 20130511 recorded in the contiguous US. These waveforms sample the Hawaiian ULVZ. The data used to retrain the DAE that is used is indicated by the titles. In a) traces are individually normalised such that the maximum amplitude corresponds to 0.75° azimuth, and traces are plotted rounded to the nearest degree of azimuth. The amplitudes in panels b) - d) are consistent with corresponding waveforms in panel a). The shaded blue and red regions are used for calculating the RMS amplitude of the noise and the signal, respectively.

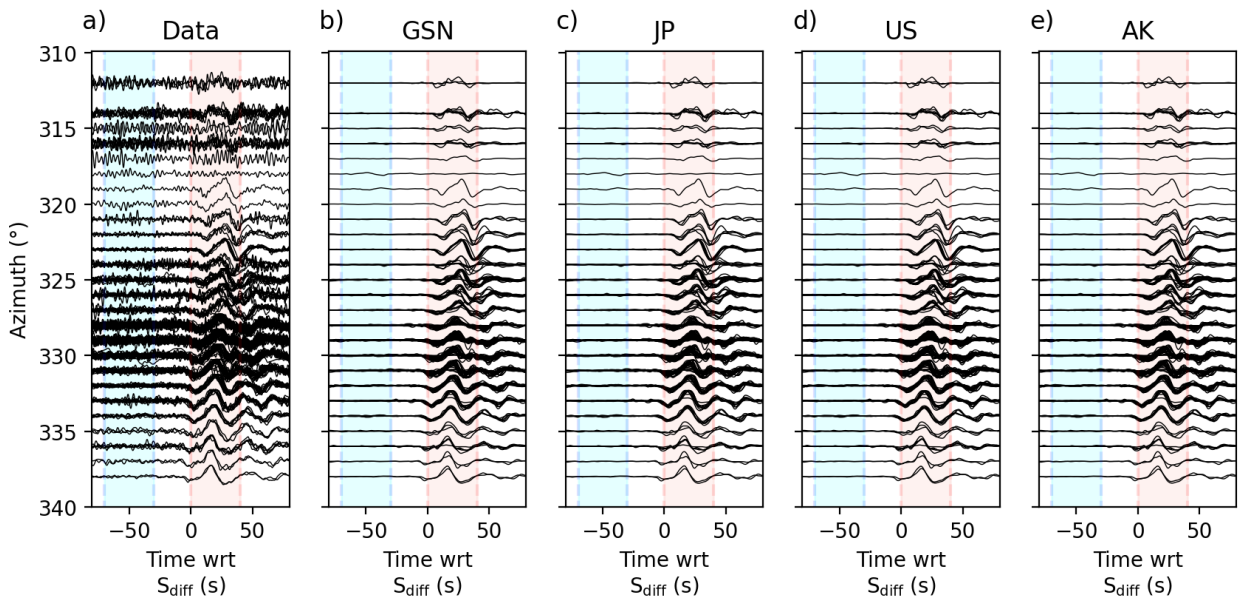


Figure S14: As for Figure S13 but for event 20161225 recorded in Alaska. These waveforms sample the Galápagos ULVZ.

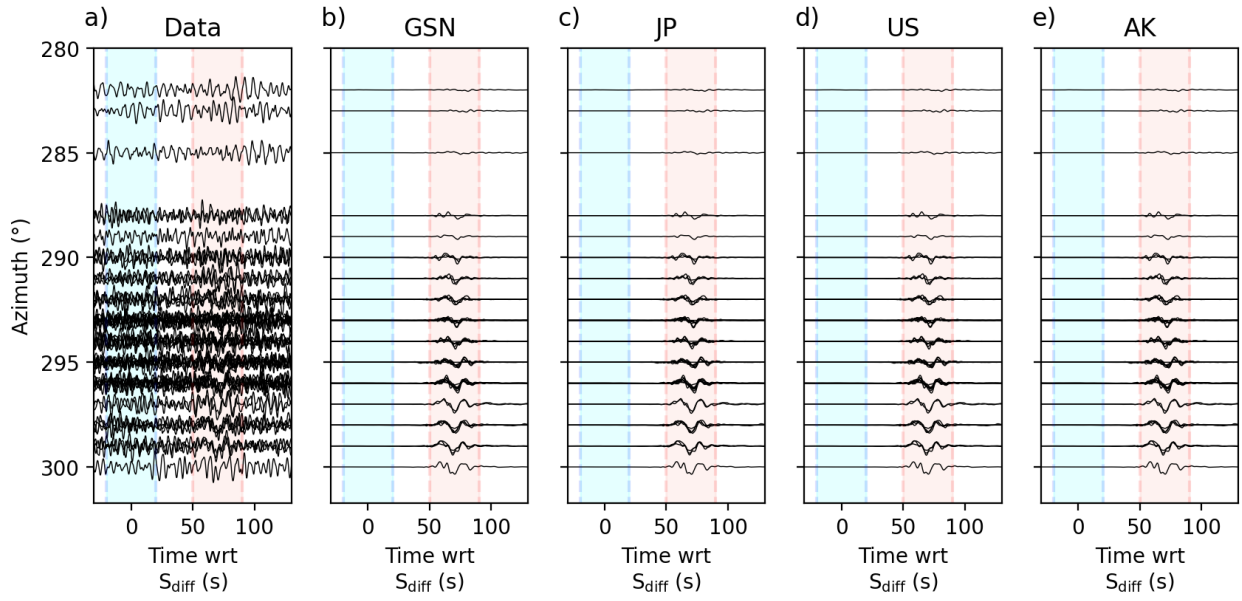


Figure S15: As for Figure S13 but for event 20090917 recorded in Japan. These waveforms sample the Hawaiian ULVZ. Note that as the waveforms are severely delayed due to the Pacific LLVP.

Section S7: Further synthetic specificity examples

In this section we show more examples of how retraining with AxiSEM3D synthetics affects the results. Specifically we show two examples where the results are not so starkly positive as in Figure 8 of the main paper. Figure S16 shows the results for Event 20160831 filtered 6.8 - 13.6 s – this event samples the Hawaiian ULVZ. The results for this event broadly mirror what is shown in the main paper, but the increase in performance when using AxiSEM3D synthetics is less. Figure S17 shows the results for Event 20161225 filtered 10.2 - 20.4 s – this event samples the Galápagos ULVZ. For this event, using AxiSEM3D synthetics has little effect on the ratio of $S_{\text{diff}+}$ to S_{diff} , but does marginally increase the SNR of S_{diff} to noise. We speculate that the ULVZ synthetics are too specific to ensure better extraction across all ULVZs, particularly those that are unlike the ULVZ in the single simulation that we ran.

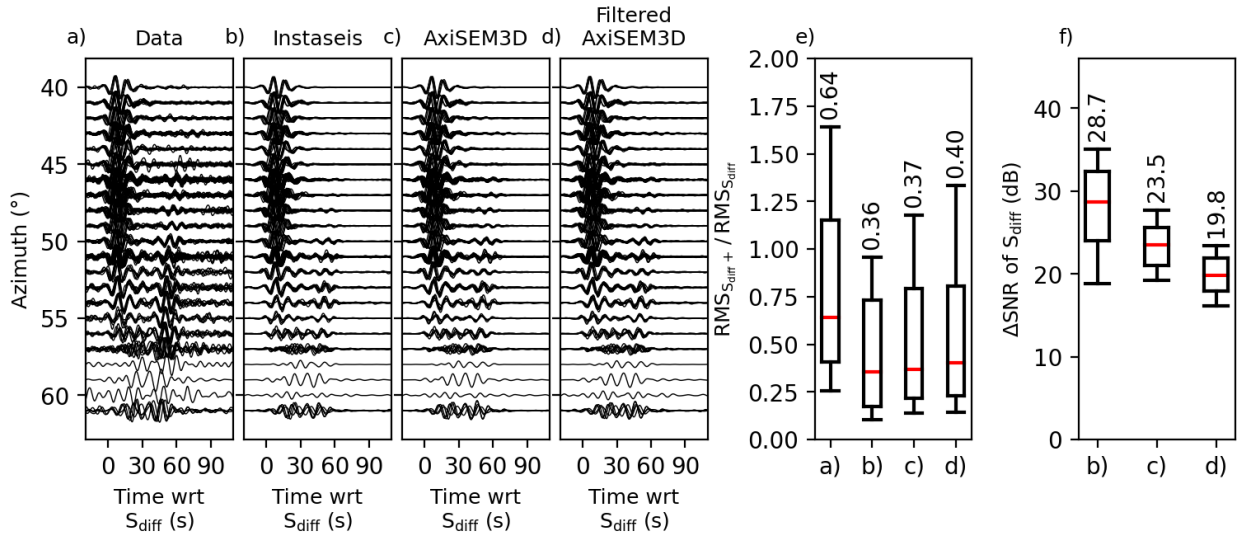


Figure S16: As for Figure 8 in the main paper, but for Event 20160831 filtered 6.8 - 13.6 s. a) The original data with each trace individually normalised such that the maximum amplitude corresponds to 0.75° azimuth, and traces are plotted rounded to the nearest degree of azimuth, b) denoised with the model trained with Instaseis synthetics, c) denoised with the model retrained with AxiSEM3D synthetics, and d) denoised with the model retrained with filtered AxiSEM3D synthetics. e) The ratios of the RMS of $S_{\text{diff}+}$ and S_{diff} for the waveforms in panels a) - d). The median is shown in red, the edges of the boxes are the 25th and 75th percentile, and the ends of the arms are the 10th and 90th percentile. The value of the median is shown above. f) As for e) but showing the improvement in SNR for S_{diff} in decibels for panels b) - d) relative to a). Absolute amplitudes in panels b) - d) are consistent with panel a).

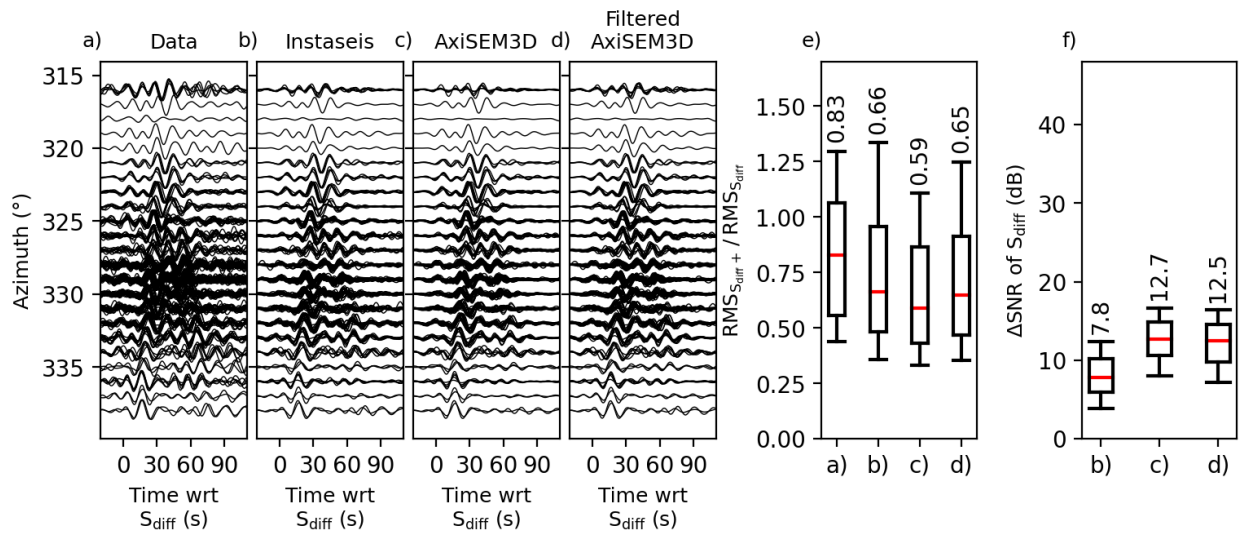


Figure S17: As for Figure S16 but for Event 20161225 filtered 10.2 - 20.4 s.

References

- Leng, K., T. Nissen-Meyer, and M. van Driel, Efficient global wave propagation adapted to 3-D structural complexity: a pseudospectral/spectral-element approach, *Geophysical Supplements to the Monthly Notices of the Royal Astronomical Society*, 207(3), 1700–1721, doi:10.1093/gji/ggw363, 2016.
- Leng, K., T. Nissen-Meyer, M. Van Driel, K. Hosseini, and D. Al-Attar, AxiSEM3D: broad-band seismic wavefields in 3-D global earth models with undulating discontinuities, *Geophysical Journal International*, 217(3), 2125–2146, doi:10.1093/gji/ggz092, 2019.
- Russell, S., J. K. Magali, K. Vallenton, and C. Thomas, The effect of source-side subduction on PKP differential times and implications for inner core anisotropy, *Physics of the Earth and Planetary Interiors*, p. 107382, doi:10.1016/j.pepi.2025.107382, 2025.